学位申請論文

竹 見 哲 也

主論文

Studies on the Structure, Evolution, and Maintenance Mechanism of a Severe Squall Line in an Arid Region

by

Tetsuya Takemi

December 1998

Abstract

Organized convective cloud systems appear to rarely occur in arid regions because of a low moisture content. They can actually, however, develop in arid regions if a certain condition is satisfied. In the present thesis, the structure, evolution, and maintenance mechanism of a severe squall line in an arid region was investigated observationally and numerically.

The observational study described the structure and evolution of a long-lived squall line that developed over the arid region in China on 5 May 1993 and caused widespread severe dust storms. This squall line evolved in a dry environment characterized by a high level of free convection (LFC) of about 5 km above the ground level. In the pre-storm environment, a mixed layer developed, and its maximum depth was estimated as about 4.3 km. The role of this deep mixed layer in the squall-line evolution was proposed. The growth of the deep mixed layer decreases the difference between the height of the mixed-layer top and the LFC and reduces the energy required to lift the mixed-layer air above the LFC. The surface cold-air pool emanated from the squall line provides the required lifting at its leading edge. Furthermore, the dry mixed layer is favorable for the evaporation of falling precipitation. Thus, the observed squall line had a strong cold pool, produced little precipitation, and evolved in the dry environment.

One-dimensional modeling of rain evaporation showed that a large amount of rain was evaporated in a dry, deep mixed layer typical of the arid region in China. The amount of evaporated rain varied widely according to rain intensity and fall distance from the top of the mixed layer. With a constant amount of total rain, the amount of evaporated rain increased significantly with rain intensity. For severe squall lines, rain falling through the subcloud layer is likely to completely evaporate.

Two-dimensional numerical experiments investigated the mechanisms for the development and maintenance of squall lines in dry environments. The effects of the mixed-layer depth and the vertical moisture profile in the mixed layer were focused on. The experiments showed that a deep mixed layer is indispensable for the squall-line development, and that a moisture profile nearly constant with height is favorable for the squall-line maintenance. The most persistent squall line developed in the condition of a well-mixed moisture profile within a deep mixed layer. Although in this condition the convective available potential energy (CAPE) for the surface air parcel was not large, air parcels in the upper part of the mixed layer ahead of a surface cold pool had moderate CAPE values, and the differences between the source levels of these parcels and their LFCs were very small. These parcels were lifted to the upper troposphere, thus contributing to the formation of clouds. On the other hand, the parcels in the lower mixed layer were transported rearward, contributing to the intensification of the cold pool. The vertical distribution of CAPE in the mixed layer affects the dynamics of the squall lines in dry environments.

Squall lines develop and persist in dry environments if the mixed layer is sufficiently deep and if the moisture is well-mixed vertically within the layer. This condition is sometimes found in the arid region of China and other arid regions in the world. Therefore, the mechanisms described in this thesis can be applied to linearly-organized convective systems in these regions.

Contents

Chapter 1

Introduction

A squall line is defined as any non-frontal line or narrow band of active thunderstorms (Huschke 1959), and is among the most outstanding systems in mesoscale meteorological phenomena. It has a much longer lifetime than a commonly observed cumulonimbus cloud and often causes severe local storms. Thus, squall lines have been studied extensively for many years, both observationally and numerically. They have been typically observed in tropical and extratropical humid climate regions.

On the other hand, squall lines in dry environments have not been well documented. Organized convective systems appear to rarely occur in arid regions because of a low moisture content. However, convective systems can actually develop in dry environments if a certain condition is satisfied. In the present study, structure, evolution, and mechanisms for maintenance of a squall line in an arid region is investigated through observational data analysis and numerical experiments.

In this chapter, first the geography and climate of the arid region in China is briefly reviewed by incorporating the recent studies during the Sino-Japanese cooperative research program, HEIFE[1], which was carried out in an arid region in northwest China (see Fig. 1.1). Next, dust storms in the region are reviewed, and finally the purpose of the present study is given.

1.1 Geography and climate overview of the arid region in China

In northwest China, arid regions extend from the Taklimakan Desert to the Gobi Desert. These deserts are located in a midlatitude zone along the 40°N latitude and located to the south of the Tibetan Plateau. The elevation of these regions is relatively high: 1000-1500 m above the mean sea level (MSL). Figure 1.1 shows the deserts and its surrounding regions. The Qilian Mountains higher than 3000 m above MSL exist just to the south of the HEIFE area.

The desert in China is distinct from subtropical dry regions in northern Africa, the Middle East,

[1]The purpose of HEIFE (the Heife River Field Experiment, 1989-1993) was to clarify the atmosphere-land surface interaction processes in a desert region (Mitsuta 1988).

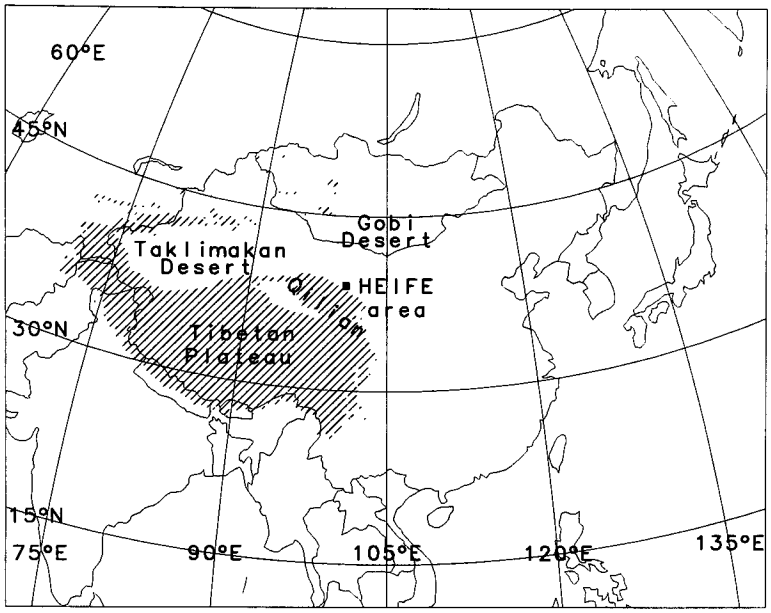

FIG. 1.1: Map of China and its surrounding area. The hatched region denotes elevations of higher than 3000 m above mean sea level.

Pakistan and northwestern India, Mexico, southern Africa, and Australia. While the subtropical dryness is due to the subsidence associated with the Hadley circulation, midlatitude aridity is controlled by another mechanism (Hartmann 1994). Broccoli and Manabe (1992) investigated the mechanism for maintaining midlatitude aridity by using a global climate model and suggested that mountains are responsible for the existence of midlatitude arid climate. For the Chinese desert, the Tibetan Plateau plays a role.

Owing to the location of a midlatitude zone, the arid regions in northwest China are affected by traveling disturbances associated with the midlatitude westerlies. There are frequent cyclogenesis events over the Gobi Desert, with peak frequencies from April to May and from August to September (Chen et al. 1991). This cyclone activity characterizes weather in the arid region. In summer, frontal cloud systems associated with cyclones frequently pass over the desert area, and these cloud systems produce precipitation in the area (Itano 1997). As a result, the precipitation in summer amounts to 50-70% of the annual precipitation (Yatagai and Yasunari 1995). The atmosphere in summer is relatively humid in a year, and the surface precipitation is observed when the relative humidity in a subcloud layer exceeds 60% (Itano 1998). On the other hand, in spring the atmosphere is very dry, and little precipitation occurs. Instead, the cyclone activity is related to dust storms in this season.

The annual precipitation in the Gobi Desert is around 100 mm, while the annual precipitation over the Qilian Mountains is as much as 600 m (Itano 1997). In fact, the annual precipitation over the HEIFE area correlates almost linearly with surface elevation (Itano 1997).

1.2 Dust storms in northwest China

The arid and semi-arid regions in China often suffer from dust storms that blow up sand particles and dust from the ground. A dust storm is characterized by a visibility of less than 1 km. In the Gobi Desert, dust storms occur 20-30 times in a year and are most frequent in spring (Mitsuta 1988; Parungo et al. 1994). These dust storms contribute to cause yellow wind phenomena over East Asia in spring.

The frequent occurrence of dust storms in spring can be attributed to the frequent cyclogenesis over the Gobi Desert. In spring, ground temperatures increase to over 50°C during daytime owing to strong surface heating (Kato et al. 1992), and the air and ground are very dry. Thus, sand particles at the ground are susceptible to erosion by strong winds associated with cyclones.

Although dust storms are frequent, extremely severe dust storms that badly affect agriculture and human lives are rare: only once or twice in a ten-year period. Once such a severe storm occurs, it causes a heavy disaster and can be a major source of yellow wind phenomena. This kind of severe dust storm is called "black storm" in China. Black storms are characterized by a visibility of less than 50 m and a wind speed of greater than $25\,\mathrm{m\,s^{-1}}$ and are reported to occur in spring (Table 1 of Mitsuta et al. 1995b).

Severe dust storms are often observed as a dust-laden gust front. Such gust fronts have been found in Sudan (Sutton 1925; Farquharson 1937; Simpson 1969; Lawson 1971; Nalivkin 1983), in Niger (Ohno 1994), in the United States (Mattice 1935; Idso et al. 1972), and in China (Mitsuta et al. 1995b).

1.3 Purpose of the study

On 5 May 1993 a black storm occurred over the arid region in northwest China (see Fig. 1.2). The storm traveled as far as 500 km, caused widespread damages over the region, and killed 49 people. Mitsuta et al. (1995b) suggested that this storm is induced by a series of downbursts emanating from a rapidly propagating, long-lived squall line. This squall line persisted for a period longer than six hours in spite of an extremely dry environment.

Generally, organized convective systems evolve in an environment having a sufficient water vapor content and potentially unstable air in the lower troposphere. Thus, dry environments seem to be unfavorable for the development of moist convection. A squall line did, however, develop and persist over the desert region on 5 May 1993. A question is raised here as to why the squall line developed and persisted in such a dry environment. The squall lines of this kind have not been well documented. Understanding the characteristics of the squall line over the arid region in China will provide important information about the occurrence of not only dust storms but also yellow wind phenomena, and is thereby expected to contribute to mitigating disastrous damages over the region. In the present study, the structure and evolution of the squall line on 5 May 1993 are described from the observational data, and the mechanisms for the development and maintenance of squall lines in dry environments are shown by numerical experiments.

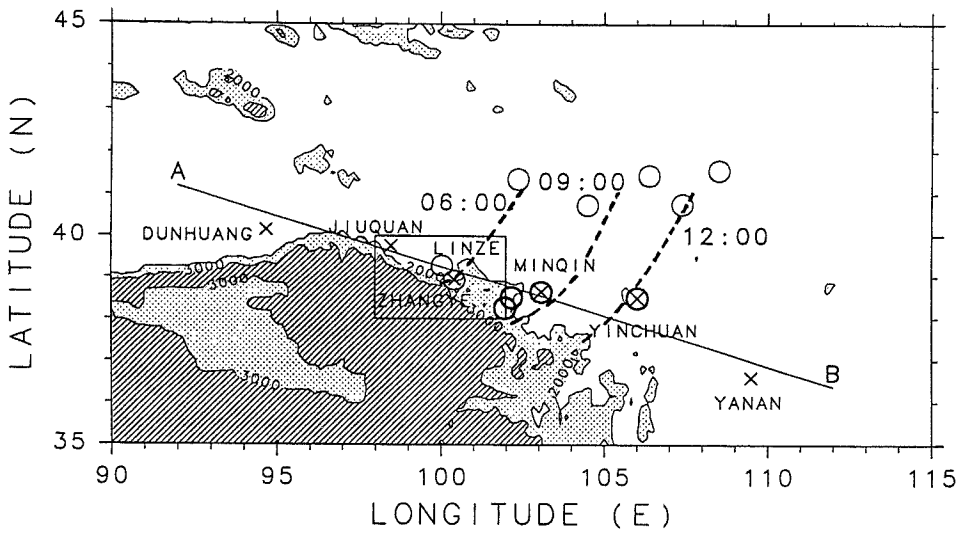

FIG. 1.2: Map of the arid region in northwest China. The stippled region represents elevations between 2000-3000 m MSL, and the hatched region higher than 3000 m MSL. Aerological observation stations are denoted by crosses. The stations observed dust storms are indicated by thin open circles, and those observed black storms by bold open circles. The dashed lines labeled with times (UTC) represent the three-hourly position of the leading edge of the squall line. The rectangular box denotes the HEIFE area.

The structure and evolution of midlatitude squall lines have been documented in detail since the early work by Newton (1950), Newton and Newton (1959), and others. Later, extensive studies revealed the internal circulation of a squall line; this was summarized in the conceptual model presented by Houze et al. (1989). This conceptual model shows an active convective region near the leading edge of the squall line, with a region of trailing stratiform rain extending to the rear of the system. Beneath the convective region, evaporatively cooled air resulting from convective downdrafts creates a surface cold-air pool. This cold pool plays an important role in maintaining the squall line through interacting with the ambient vertically-sheared winds to produce a convective cell at the gust front (Thorpe et al. 1982; Rotunno et al. 1988; Weisman et al. 1988; Fovell and Ogura 1988).

The conceptual model of Houze et al. (1989) was based on many observational studies of the squall lines over the United States and tropical regions. On the other hand, few case studies have been conducted on squall lines over dry regions; there are several studies on those over the semi-arid High Plains in the United States (eg., Schmidt and Cotton 1989; Fankhauser et al. 1992; Grady and Verlinde 1997).

The environment of the semi-arid High Plains are characterized by a rather high lifting condensation level (LCL), a high level of free convection (LFC) as well, and low convective available potential energy (CAPE) compared to the values in the Oklahoma area reported in Bluestein and Jain (1985), Bluestein et al. (1987), and Houze et al. (1990). Fankhauser et al. (1992) showed the boundary layer ahead of a

squall line was well mixed with an adiabatic lapse rate. This boundary layer was similar to a mixed layer (ML) structure typical of the High Plains (Mahrt 1976). In this semi-arid region, a deep dry-adiabatic layer sometimes develops up to near the 500 hPa level, and such layers are favorable for dry downbursts (Wakimoto 1985). Under dry conditions, evaporation of falling precipitation is expected to readily occur in a convective system, leading to the rapid development of a surface cold pool (Sawyer 1946; Braham 1952; Krumm 1954; Kamburova and Ludlam 1966). At the leading edge of the cold pool, updrafts occur. What should be noted here is that some mechanism is required to sustain deep convection at the leading edge of a cold pool against the high LFC conditions that are unfavorable for the development of deep convection. Ogura and Chen (1977) showed that a well-defined ML developed at low levels in a pre-squall environment, and that this ML height gradually increased and became close to the LCL. They therefore suggested that only a small lifting at the ML top would be necessary to generate convective clouds.

In the desert region of northwest China, a deep ML develops, sometimes up to 4 km above the ground level (AGL), during the summer season (Gamo 1996). Such a deep ML can be found in the afternoon (1200 UTC[2]) also in spring (Fig. 1.3). During warmer seasons, particularly in May and June, sensible

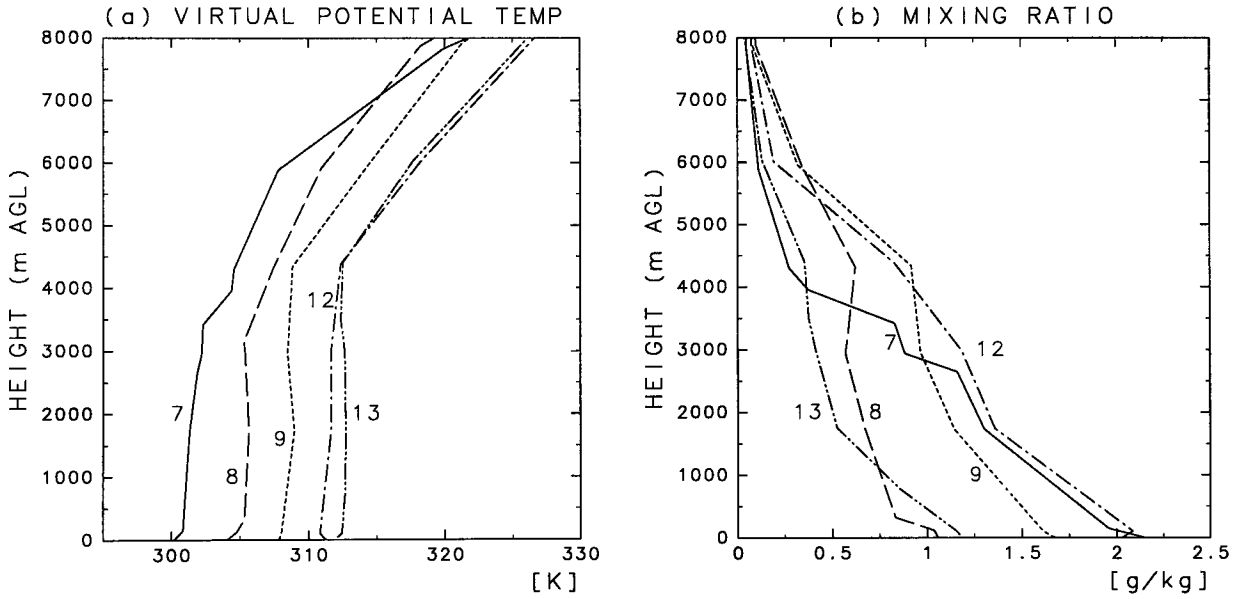

FIG. 1.3: The vertical profiles of virtual potential temperature and water vapor mixing ratio at Minqin at 1200 UTC on days when a deep mixed layer developed in May 1991. The numerals labeling the lines indicate the selected days.

heat flux from the surface is very strong (Mitsuta et al. 1995a), and can contribute to the increased ML height. At the same time, the LFC is very high. Itano (1997) suggested that the high LFC condition is unfavorable for lifting the air parcel in the atmospheric boundary layer (ABL) up to the LCL and LFC,

[2]The local time in China is 8 hour plus UTC.

and that deep cumulus convection does not develop without large-scale external forcings. However, if a deep ML develops, the unfavorable condition of high LFC seems to be eliminated.

One of the important characteristics of the ML over arid and semi-arid regions is that moisture content often decreases with height (Mahrt 1976; Wakimoto 1985; Crook 1996; Knupp 1996), while the layers are well-mixed in terms of virtual potential temperature. A similar characteristic is seen also in the arid region of China (Fig. 1.3). It should be noted that the vertical profile of moisture in the ML may affect the development of convection because the LCL varies with the originating level of a parcel in the ML if the moisture content is not constant with height.

The dynamics of squall lines in sufficiently unstable environments have been investigated by idealized numerical experiments (Thorpe et al. 1982; Dudhia et al. 1987; Rotunno et al. 1988; Weisman et al. 1988; Nicholls et al. 1988; Fovell and Ogura 1988, 1989; Lafore and Moncrieff 1989; Garner and Thorpe 1992; Weisman 1992; Skamarock et al. 1994; Fovell and Tan 1998, and others). These studies have focused on the interaction between the squall-line circulation and the environmental vertical wind shear. Rotunno et al. (1988) investigated dynamics of long-lived squall lines and showed that the essential mechanism that sustains squall lines is the interaction between the circulation induced by the surface cold-air pool and the ambient low-level shear. They argued this interaction by considering the horizontal component (parallel to the squall line) of vorticity. The tilt of updraft at the leading edge of the cold pool is determined by the relative strengths of the vorticity generated baroclinically at the cold pool edge and the vorticity inherent in the ambient shear. If the strengths of these two vorticities are equally matched, deep lifting is produced at the cold pool edge, resulting in the production of strong convective cells in the squall line.

Although the wind shear conditions have been investigated extensively, thermodynamic conditions have not. Weisman (1992) examined the effect of low-level mixing ratio on the squall-line evolution in environments having large potential instability. He examined, however, neither dry conditions nor the low-level vertical profile of moisture. Droegemeier and Wilhelmson (1985) investigated the effects of low-level moisture on a cold outflow and concluded that a decrease in the low-level moisture leads to weaker clouds along the outflow boundary. In their study, the vertically integrated moisture content for each experiment was not the same with each other, and the drier simulation produced only weaker convection. Crook (1996) investigated the sensitivity of moist convection to potential temperature and moisture structures within a boundary layer. The sensitivity was defined as the typical variability estimated from field experiments in Colorado. His results showed that the initial stage of convection development was most sensitive to the temperature and moisture differences between the values measured at the surface and in the boundary layer, while convection was not so sensitive to the shape of moisture profile in the boundary layer. In his study, the initial stage of convection development was focused on; but the mature stage of organized convective systems was not investigated. Thus, it is still not known how the boundary-layer thermodynamic structure affects the development and maintenance of squall lines in their mature stage.

In light of the above reviews, we will examine in chapter 2 the observational data of the 5 May 1993 squall line and organize them to show the characteristic features of a squall line in a dry environment. The effects of low-level dry conditions are focused on. As a next step, we will carry out numerical experiments to show the mechanisms responsible for the development and maintenance of squall lines in dry environments. Before going on to the experiments by a cloud model, we will use a simple one-dimensional (1D) model in chapter 3 to examine the effect of evaporation to influence the amount of rain and the other variables in an extremely dry condition. In chapter 4, we will present two-dimensional numerical experiments to investigate the squall-line dynamics in dry environments. In these experiments, we will focus on the sensitivities of the squall lines to boundary-layer thermodynamic structure: the ML height and the vertical moisture profile within the ML. Finally, in chapter 5 we will summarize and conclude the present study.

The present thesis was based on the following original papers:

- Takemi (1998a, hereafter T98a),
- Takemi (1997, hereafter T97),
- Takemi (1998b, hereafter T98b),
- Takemi and Satomura (1998, hereafter TS98).

The abbreviations in the parentheses will be used in this thesis when the above papers are referred. The author made all the investigations in TS98, with advice and suggestions from Dr. Takehiko Satomura. Each chapter of this thesis includes the contents of the above papers as follows:

chapter 2 — T98a and T97,

chapter 3 — T98b,

chapter 4 — TS98.

Chapter 2

Structure and evolution of the observed squall line

2.1 System overview

2.1.1 Synoptic conditions

Figure 2.1 shows a satellite (GMS-4) IR image at 0930 UTC. A wide, banded cloud system is seen in

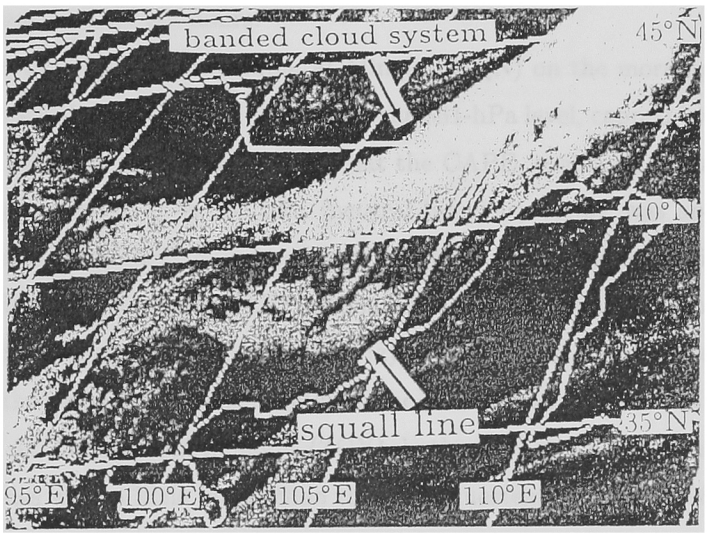

FIG. 2.1: A GMS-4 IR image over China at 0930 UTC. The squall line and the banded cloud system are indicated by arrows.

Fig. 2.1. A surface cold front is identified as a sharp gradient in temperature in the 850-hPa contour chart at 1200 UTC (Fig. 2.2). This cold front corresponds to the leading edge of the cloud band as shown

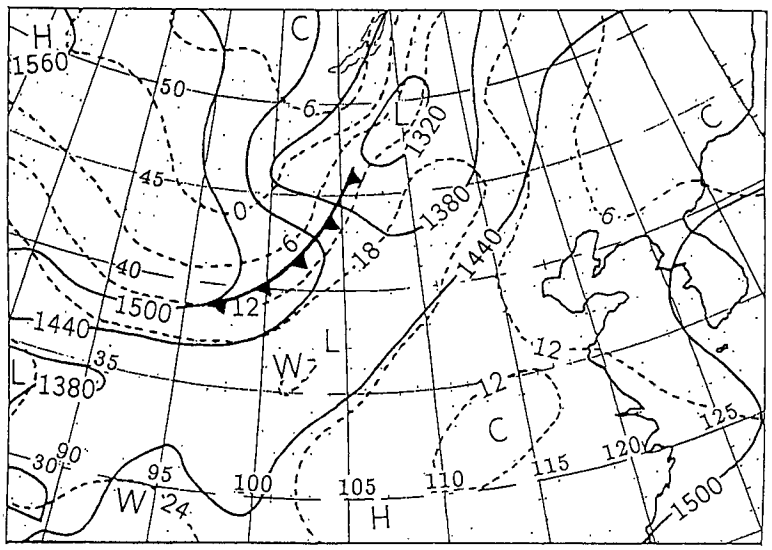

FIG. 2.2: 850-hPa level weather chart at 1200 UTC, analyzed by Japan Meteorological Agency. The geopotential heights are contoured by solid lines (every 60 m) and the temperatures by dashed lines (every 6°C). The barbed line indicates the surface cold front.

in Fig. 2.1. In IR images, the squall line was first identified at 0530 UTC, and began to evolve into a linearly-organized cloud system ahead of the cold frontal cloud band (Fig. 2.1). The squall line moved from 304° with an average speed of about $19\,\mathrm{m\,s^{-1}}$ The linear structure of the squall line cloud was traced in the IR images for over six hours.

In Figs. 2.3a and b that show the sounding at Minqin (MQN) on the morning (0000 UTC) of 5 May 1993, an absolutely stable stratification is seen below the 831-hPa level, capped by a convectively unstable layer ($\partial\theta_e/\partial z < 0$). The morning profile showed that the CAPE, evaluated by raising a parcel from 831 hPa (top of the surface inversion) to 285 hPa (neutral buoyancy level), was approximately $450\,\mathrm{J\,kg^{-1}}$ This value was not so large as those found in severe squall lines over Oklahoma in spring (Bluestein and Jain 1985). In the afternoon, however, CAPE estimated by Mitsuta et al. (1995b) was $1340\,\mathrm{J\,kg^{-1}}$ This large CAPE reflected the destabilization of surface layer due to strong surface heating.

The magnitude of the vertical wind shear between the surface and the 400-hPa level at MQN was $4.7 \times 10^{-3}\,\mathrm{s^{-1}}$ (Fig. 2.3c). At Jiuquan and Zhangye (ZGY), both of the shear magnitudes were $4.9 \times 10^{-3}\,\mathrm{s^{-1}}$ These shear magnitudes were a little larger than those in Bluestein and Jain (1985). On the other hand, shears in low levels were relatively small. For instance, the shear magnitude between the surface and the 700-hPa level (about 1.7 km AGL) at MQN was $1.7 \times 10^{-3}\,\mathrm{s^{-1}}$

2.1.2 Surface changes associated with the passage of the squall line

Dust storms and black storms were observed over a wide area on 5 May 1993 (Fig. 1.2). In this event,

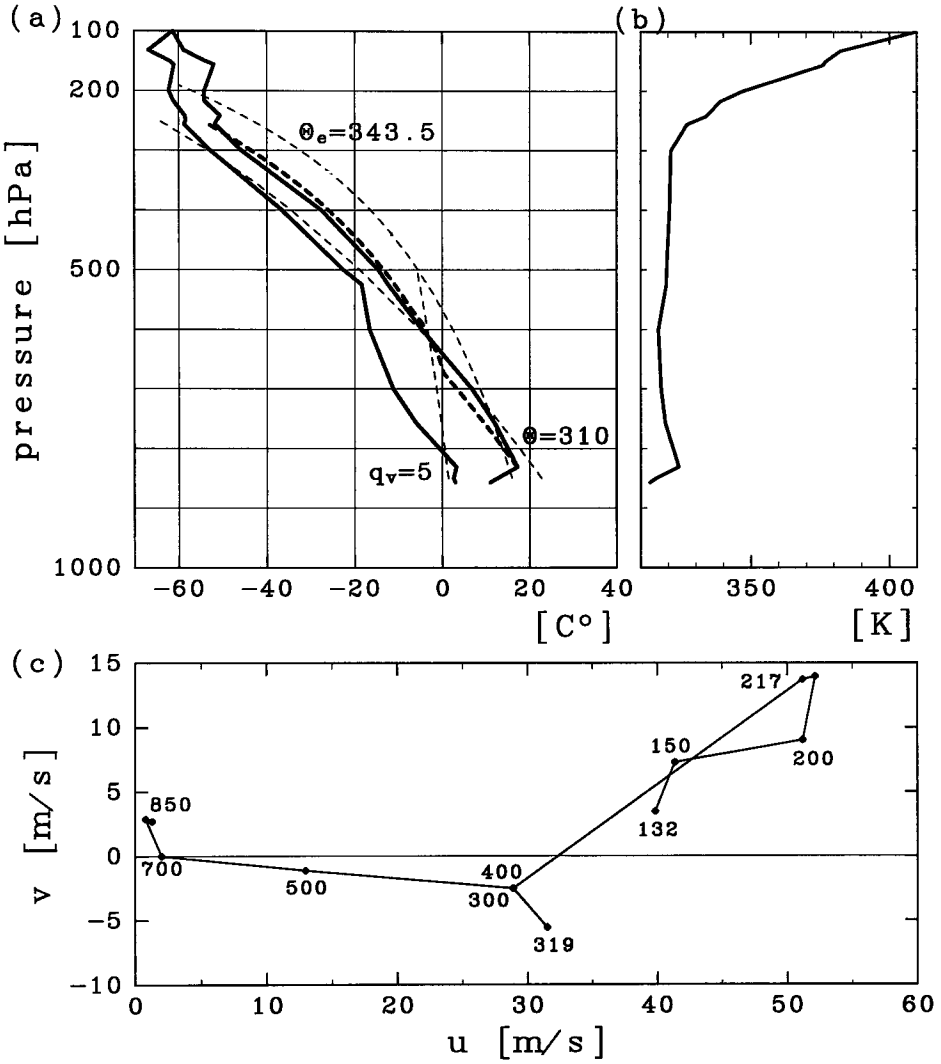

FIG. 2.3: Thermodynamic diagrams and wind hodograph at Minqin at 0000 UTC 5 May 1993. (a) Temperature and dewpoint profiles are represented by the bold solid line. The parcel path used to estimate CAPE is shown by bold dotted line. The dry (θ = 310 K) and moist (θ_e = 343.5 K) adiabats, and constant mixing ratio (q_v = 5 g kg^{-1}) are indicated by the thin labeled dotted lines. (b) The vertical profile of equivalent potential temperature θ_e. (c) Wind hodograph. The pressure levels (hPa) are labeled along the line.

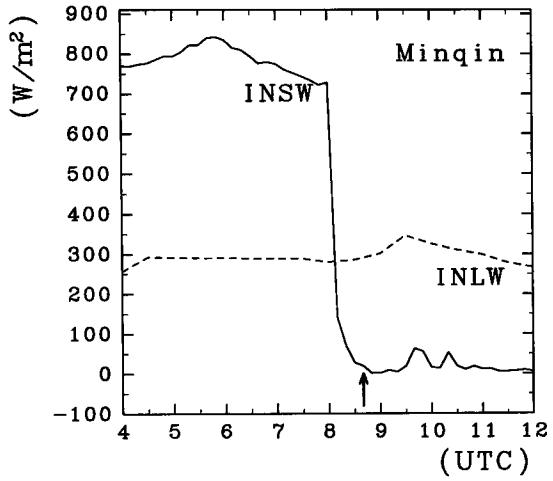

FIG. 2.4: Incoming short wave radiation (INSW) and incoming long wave radiation (INLW) at MQN on 5 May 1993. The arrow indicates the time of the gust front arrival.

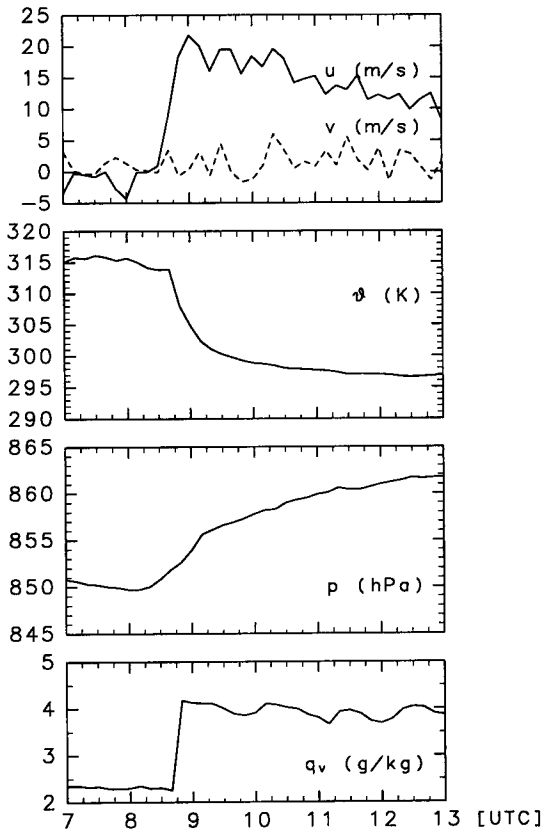

FIG. 2.5: Time series of surface variables observed at MQN AWS. Wind components u and v indicate parallel and normal to the squall-line motion, respectively.

the peak gust reached $37.9\,\mathrm{m\,s^{-1}}$ at ZGY, and $34\,\mathrm{m\,s^{-1}}$ at Jinchang that is near MQN. The visibility dropped to almost zero in the black storm areas, as indicated in the radiation data (Fig. 2.4). Surface observations by the automatic weather stations (AWSs) of the HEIFE network clearly marked the passage of the squall line (Fig. 2.5). With the arrival of the gust front (0840 UTC), the potential temperature (θ) decreased as the pressure (p) began to rise. The water vapor mixing ratio (q_v) simultaneously increased from 2.3 to $4.2\,\mathrm{g\,kg^{-1}}$ This increase in q_v probably results from the evaporation of falling precipitation. The strong wind speed lasted for more than two hours. During the two hours after the passage of the gust front, several major peaks in the u-component are found. Similar wind speed changes were also observed at the Linze (LNZ) AWS (see Fig. 9d of Mitsuta et al. 1995b).

In the present event, almost no rain was observed at the ground. Instead, q_v increased after the passage of the gust front. This fact sharply contrasts with those found in rain storms that typically develop over humid regions. The increase in q_v has also been reported for other dust storms over arid

regions (Farquharson 1937; Idso et al. 1972), and appears to be a common feature of the dust storms.

2.2 Squall line structure

2.2.1 Vertical cross section

Vertical cross sections of the squall line and its environment along the line A-B shown in Fig. 1.2 were constructed by using twice daily aerological soundings at six stations.

In the vertical cross section of the pre-storm environment at 0000 UTC (Fig. 2.6), a region of low equivalent potential temperature (θ_e) is seen near the ground, demonstrating that the inversion layer extended horizontally over the region. Above this layer, a neutral-to-weakly unstable layer is seen around MQN.

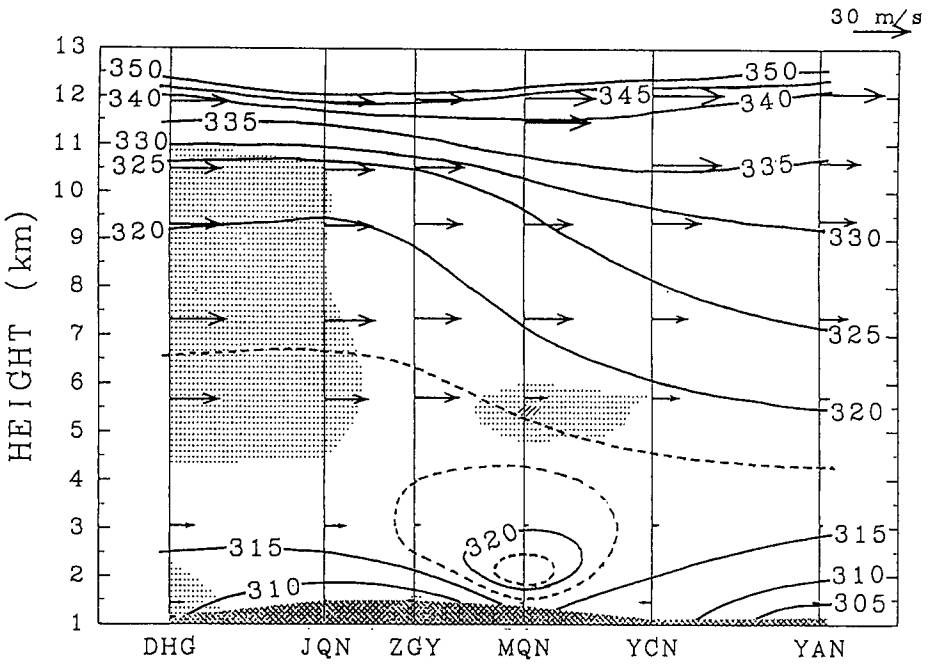

FIG. 2.6: Vertical cross section at 0000 UTC, oriented along the line A-B shown in Fig. 1.2. θ_e is contoured every 5 K, with auxiliary contours every 2.5 K (dotted lines). The stippled and hatched regions denote relative humidity of 50-60% and of greater than 60%, respectively. Vectors represent wind components parallel to the squall line motion. The unit vector is indicated in the upper right corner. The cross-hatching along the bottom represents the ground.

The vertical cross section of the squall line at 1200 UTC is shown in Fig. 2.7. A sharp horizontal θ_e gradient is seen to the west of YCN, recognized as a gust front. Ahead of the gust front, a convectively unstable layer is found at low levels (CAPE $\approx 530\,\mathrm{J\,kg^{-1}}$, LFC $\approx 4.4\,\mathrm{km}$ AGL at YCN). The pre-storm

YCN sounding showed that the vertical gradient of virtual potential temperature (θ_v) in lower levels between 850-500 hPa was about 4 K/4.3 km. This small θ_v gradient indicates the presence of a deep ML. Behind the gust front, a well-defined cold pool is seen. The propagation speed of the cold surface outflow was about 20 m s^{-1}, estimated from the surface pressure change at MQN. This value was almost the same as that estimated from the satellite images. In Fig. 2.7, a weak horizontal θ_e gradient is seen at around 800 km behind the gust front. This θ_e gradient corresponds to a synoptic-scale cold front as shown in the surface analysis (Fig. 2.2).

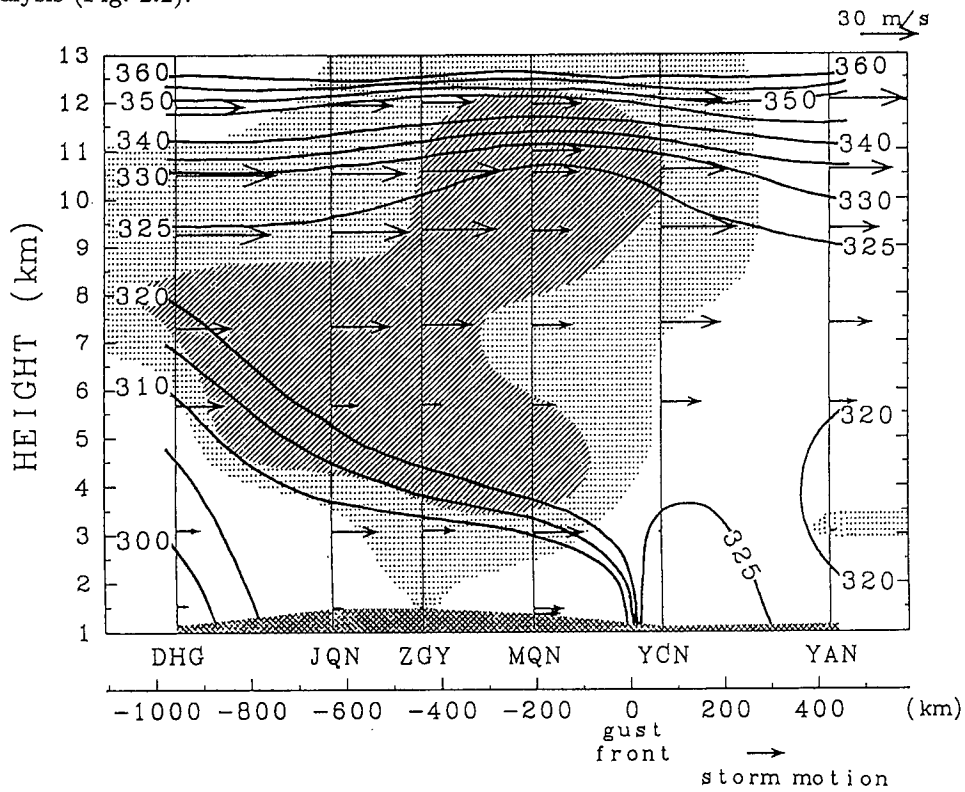

FIG. 2.7: Same as in Fig. 2.6, except for 1200 UTC. The horizontal scale displayed at the bottom indicates the distance relative to the gust front.

The vertical cross section of the present squall line appears to be similar to those found over the United States (Newton 1950; Newton and Newton 1959; Ogura and Liou 1980). It should be noted that the relative humidity in the cold pool was lower than that in the cloud area (Fig. 2.7). This fact as well as almost no observed rainfall indicates that the lower atmosphere was so dry that it could not be saturated even if all the precipitation evaporated. At ZGY far behind the gust front at 1200 UTC, the relative humidity was higher than that within the cold pool over the other stations (Fig. 2.7). Owing to this relatively moist condition, ZGY observed a little rainfall of less than 0.1 mm.

From the vertical wind profile at YCN (Fig. 2.7), the horizontal winds at low levels were very weak and had no substantial vertical shear in the direction of the squall line motion. In mid-to-upper troposphere, however, strong shear existed. The shear magnitude between 700-300 hPa was 5.6×10^{-3} s^{-1} A strong

mid-level but weak low-level shear was also found in the MQN morning wind profile as mentioned in section 2.1.1. This shear condition seems to be in contrast to the theory of Rotunno et al. (1988). Rotunno et al. stressed that sufficient low-level shear interacting with a surface cold pool is important for maintaining strong, long-lived squall lines. The present case therefore suggests another maintenance mechanism of squall lines in addition to the Rotunno et al. theory.

2.2.2 Surface convergence

The horizontal-wind convergence can be induced at the gust front of the squall line. The horizontal divergence resulting from the surface winds was computed by the method described in section 3b of T98a.

The divergence fields of the surface winds at 0600, 0900, and 1200 UTC on 5 May are shown in Fig. 2.8. At 0600 no significant convergence related to the squall line is seen. However, at 0900 a region of large convergence (greater than $10^{-4}\,s^{-1}$) is found around 104°E, 39°N. This region extends a few hundred kilometers along the southwest-northeast direction. Even at 1200 a significant convergence zone translated southeastward from 0900 is found. The wide areas of large convergence are related to the large horizontal extent of the squall line.

2.3 Pre-storm dry boundary layer

2.3.1 Estimation of the mixed-layer depth

In section 2.2.1, the presence of a deep ML in the pre-storm environment has been suggested based on the 1200 UTC sounding at YCN. During the daytime, ground temperature increased to about 50°C at MQN, while the surface air temperature to about 27°C in the afternoon (Fig. 6 of T97). This large temperature difference leads to a strong sensible heat flux. Thus, a deep ML is expected to develop. In this section, the maximum mixed-layer depth (MMD) and the LFC in the pre-storm environment are estimated. The estimates are based on a simple assumption that the growth of the ML arises from surface heating alone, and that the potential temperature within the ML is constant with height (encroachment growth, Garratt 1992).

The MMD was estimated by lifting the maximum surface θ_v to its intersection with the morning θ_v profile. This method is equivalent to that discussed in Holtzworth (1964). The LFC was estimated by lifting the maximum surface θ_e to its intersection with the morning saturated θ_e profile. This procedure was schematically illustrated in Fig. 10 of T98a. The estimations were made from the data at ZGY and MQN. The maximum values of θ_v and θ_e were defined as the means over a certain period during the daytime.

Table 2.1 summarizes the estimated values of MMD and LFC. The MMD at ZGY is lower than that at MQN, probably because the passage of the squall line over ZGY occurred early enough in the afternoon to prevent the ML from obtaining a sufficient amount of sensible heat. At MQN, the MMD is estimated

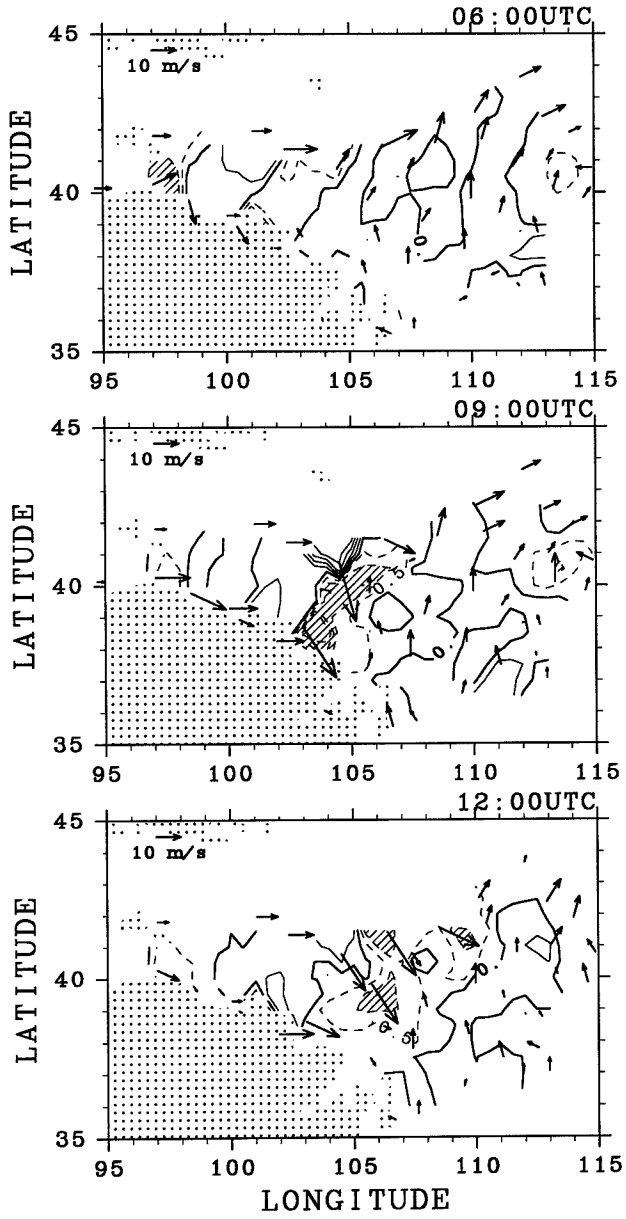

FIG. 2.8: The surface convergence/divergence field at 0600, 0900, and 1200 UTC. Values are contoured at $0.5 \times 10^{-4}\,s^{-1}$ with negative (convergence) values indicated by dashed lines and positive (divergence) by solid lines. The hatched region denotes convergence $> 10^{-4}\ s^{-1}$ The surface wind is represented by vector whose scale is given at the upper left corner of each panel. The wind observing stations are located at the roots of the vectors. Stippled regions denote elevations higher than 2000 m MSL.

as greater than 4 km, while the LFC as about 5 km. Although the estimated LFC at MQN is very high, the difference in height between the MMD and LFC is only about 700 m.

TABLE 2.1: Mean surface maximum of θ_v and θ_e, estimated maximum mixed-layer depth, and level of free convection at Zhangye and Minqin.

Site	Mean surface maximum θ_v (K)	Mean surface maximum θ_e (K)	Maximum mixed-layer depth (m AGL)	Level of free convection (m AGL)
Zhangye	309.7	321.7	1678	4090
Minqin	315.0	323.0	4267	4953

2.3.2 The role of a deep mixed layer in the squall-line evolution

The role of the deep ML in the squall-line evolution is discussed here. If the ML is high, the difference between the height of the ML top and LFC is small. The energy required to lift the ML air above the LFC thus decreases. In addition to the presence of the deep ML, mechanical forcing is required to lift the ML air above the LFC to develop deep convection. In the present squall line, lifting is probably provided by the cold surface outflow. With this forcing, the entire ML will be lifted by the depth of this cold outflow: about 2 km as shown in Fig. 2.7. The upper part of the ML thereby reaches the LFC. The wide area of the surface convergence as calculated in section 2.2.2 indicates that the lifting occurred in a large area.

The dry, deep ML also seems to be favorable for the evaporation of falling precipitation. This evaporation in turn contributes to strong downdrafts and the production of cold-air pool. In this way, the role of a deep ML seems to be a characteristic of the squall-line evolution in an arid region.

2.4 Cooling mechanism of the boundary layer

The effect of cooling by rain evaporation in the boundary layer was estimated by the following thermodynamic energy equation as:

$$C_p \frac{d \ln \theta}{dt} = \frac{1}{T} \frac{dQ}{dt}, \tag{2.1}$$

where Q is the diabatic heating, and C_p denotes the specific heat of dry air at constant pressure. Assuming that rain evaporation is the only source for the diabatic cooling, we obtain $dQ = -L_v dq_v$, where L_v is the latent heat of vaporization. Written in finite difference form, (2.1) becomes

$$\Delta \ln \theta = -\frac{L_v}{C_p T} \Delta q_v. \tag{2.2}$$

With this (2.2), evaporative cooling was estimated for the LNZ and MQN data. The pre-storm basic state was defined as the mean over the two hours just prior to the arrival of the gust front. Δq_v was defined as the deviation from the pre-storm state at the time of the gust-front arrival.

In Table 2.2, the computed potential temperature change $(\Delta\theta)_c$ is compared with the observed change $(\Delta\theta)_o$ The cooling by evaporation explains 84% of the observed total cooling at LNZ, and 68% of the observed cooling at MQN. The smaller contribution of rain evaporation to the total cooling at MQN is probably due to cold-air advection. The cold-air advection is suggested by a decrease in θ_e after the passage of the gust front, because θ_e is a conserved variable during the evaporation of rain.

TABLE 2.2: Estimates of the cooling by evaporation.

	Pre-storm		gust-front arrival		Computed	Observed	
	Mean θ	Mean q_v	θ	q_v	$(\Delta\theta)_c$	$(\Delta\theta)_o$	$(\Delta\theta)_c/(\Delta\theta)_o$
Site	(K)	($g\,kg^{-1}$)	(K)	($g\,kg^{-1}$)	(K)	(K)	(%)
Linze	309.2	3.87	306.1	4.89	-2.6	-3.1	84
Minqin	315.1	2.33	308.0	4.17	-4.8	-7.1	68

In the present case, the cloud base was very high (LCL $\approx$ 4.5 km AGL), and the temperature at the cloud base was less than 0°C. Another possible cooling mechanism at MQN is hence the melting and sublimation of precipitation. The latent heat of melting is an order of magnitude smaller than those of evaporation and sublimation. Thus, melting seems to play a minor role in cooling (estimated as about 10% of the total cooling). On the other hand, if L_v in (2.2) is replaced by the latent heat of sublimation, then $\Delta\theta = -5.4$ at MQN. This value accounts for 77% of the total cooling. The estimation appears to become improved. However, the level at which temperature was 0°C was high at MQN (about 2.8 km AGL). Thus, the evaporation of precipitation is probably the dominant process in the diabatic cooling that occurs in the subcloud layer.

2.5 Moisture source for the desert region

In Fig. 2.9, the surface moisture content on the morning (0000-1200 BST[1]) of 5 May 1993 was rather higher than that on the previous days. Moreover, the precipitable water content at MQN at 0000UTC on 5 May 1993 was 11.1 $kg\,m^{-2}$; this value was greater than the monthly mean values of April and May in 1991 (Itano 1997). Therefore, the present squall line is possibly fueled by this somewhat large amount of moisture.

Figure 2.10 shows the large-scale moisture fields and horizontal flux of moisture at the surface level. Around the south of the Gobi Desert (see around 103°E, 38°N in Fig. 2.10), water vapor mixing ratio is

[1]BST means UTC+8 hour.

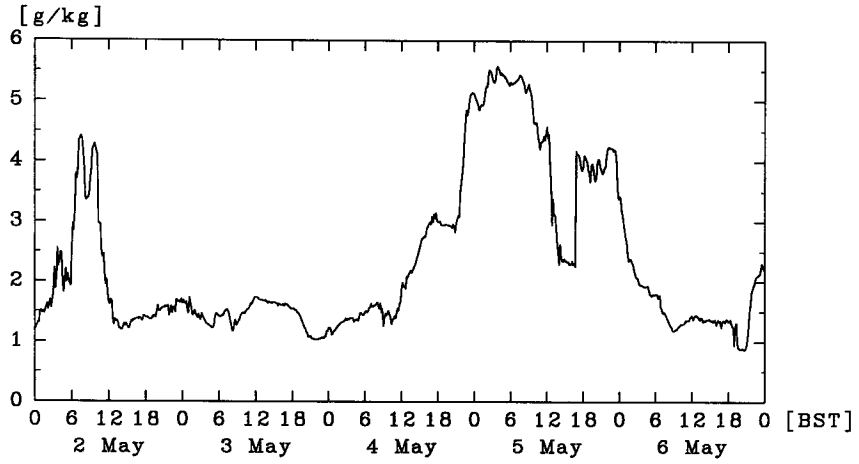

FIG. 2.9: Time series of water vapor mixing ratio at MQN AWS during 2-6 May 1993.

around $2\,\mathrm{g\,kg^{-1}}$ in the afternoon of 4 May, while it is greater than $5\,\mathrm{g\,kg^{-1}}$ in the midnight of 5 May. Nevertheless, no significant moisture flux into the desert region is found at the both times. Moreover, the field of horizontal moisture flux integrated from the surface to the 700-hPa level also does not suggest inflow to the desert region (Fig. 2.11). Thus, the large-scale wind system associated with the cold frontal activity does not seem to be relevant to the increased moisture in the desert region.

At MQN AWS, the wind direction during the nighttime between 4 and 5 May was south-southwest: this direction was from the Qilian Mountains. As shown in Fig. 2.10, a region of large moisture content over the eastern part of the Tibetan Plateau appears to advance northward to the Gobi Desert. Thus, the increased moisture at the desert during the nighttime is probably induced by the airflow from the mountains. Taking into account this airflow direction, a local circulation between the mountainous area and the desert is suggested. This local circulation possibly plays a part in increasing the moisture content in the desert region.

2.6 Similarity with other storms

In Fig. 2.5, several major peaks in the u-component at MQN are seen during about two hours after the passage of the gust front. Furthermore, there were also several reports of gusty winds over $30\,\mathrm{m\,s^{-1}}$ (section 2.1.2). In addition to these strong winds, the wind damage area extended with a major axis length of more than 500 km. These characteristics are similar to those of derecho, a widespread convectively induced windstorm. A derecho is typically observed over the continental United States during the late spring and summer, emanates from a mesoscale convective system (MCS), and causes multiple wind damages (Johns and Hirt 1987). The multiple structure in severe surface winds associated with a MCS has been reported by Fujita and Wakimoto (1981). These multiple severe winds are caused by multiple

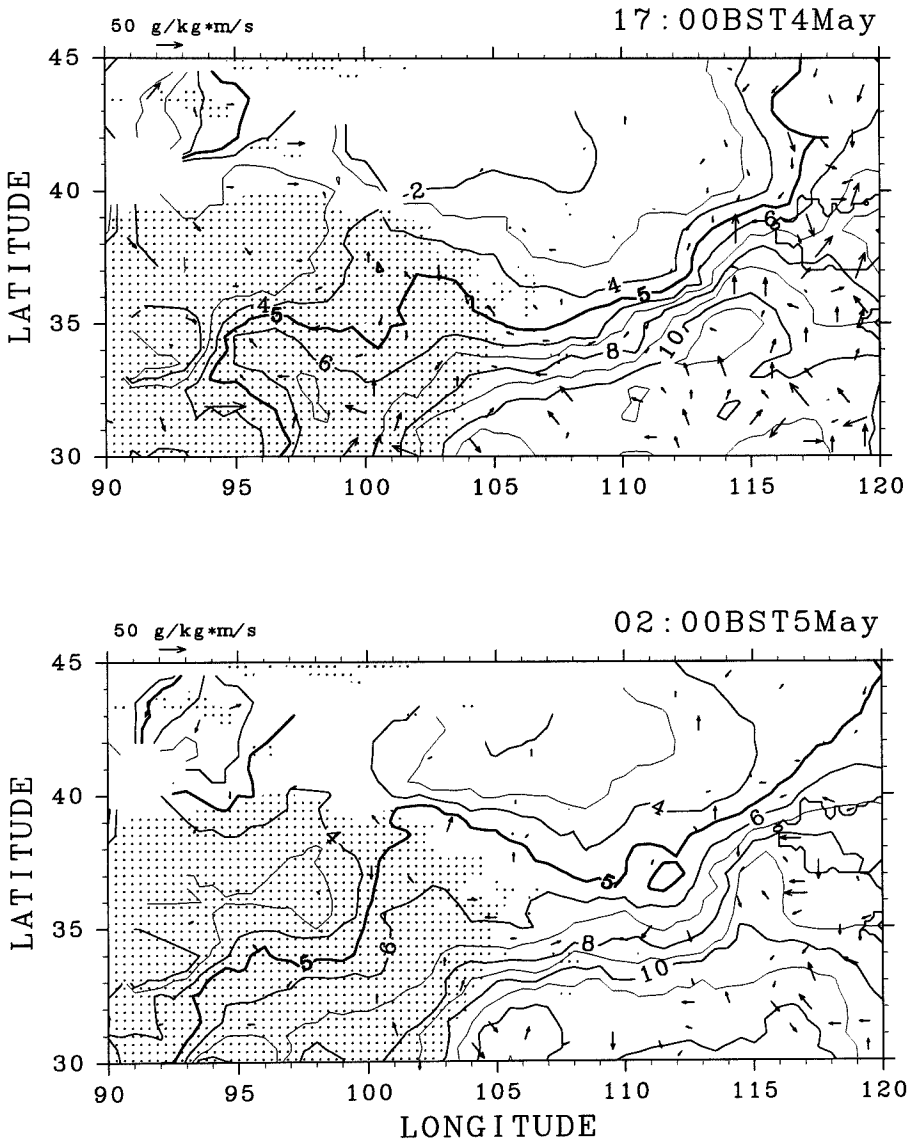

FIG. 2.10: Water vapor flux (vectors) and water vapor mixing ratio (in $g\,kg^{-1}$, contours) at the surface level at 1700 BST on 4 May (above) and at 0200 BST on 5 May (bottom). Hatched regions denote the elevations of higher than 2000 m, MSL. The unit vector is indicated in the upper left corner.

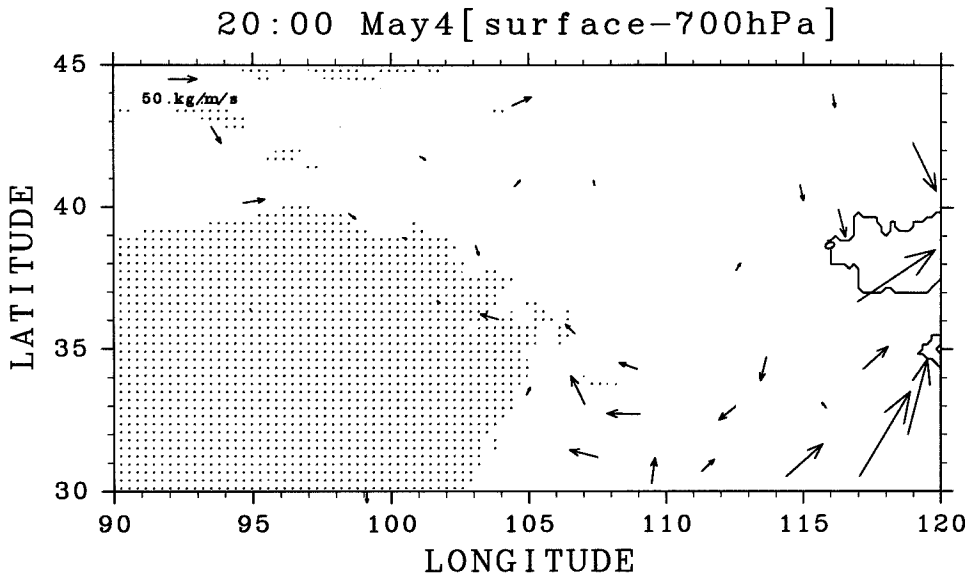

FIG. 2.11: Water vapor flux integrated between the surface and 700-hPa level at 2000 BST May 4 (vectors). A hatched region denotes the elevations of higher than 2000 m, MSL. The unit vector is indicated in the upper left corner.

downbursts within a MCS. A derecho is identified as a family of downbursts produced by a MCS (Johns and Hirt 1987). The present storm in China seems to exhibit the same characteristics as a MCS producing multiple strong downdrafts.

Chapter 3

One-dimensional modeling of rain evaporation

Owing to the sufficient depth and dryness of a ML in the arid region, the evaporation of rain can be significant. Itano (1997) investigated a rainfall event in August 1991 and showed that rainfall at the desert surface was much less than that over the adjacent high mountains in spite of the passage of an identical precipitating cloud system over the both desert and mountains regions. He attributed this strong dependence of rainfall on altitude to the evaporation of rain in a dry ABL.

In this chapter, a simple 1D model is used for investigating the evaporation of rain falling through a dry subcloud layer typical of the arid region in northwest China.

3.1 The numerical model

The framework of the present model was basically the same as that of the time-dependent model by Syono and Takeda (1962), except that rain was represented by a bulk of raindrops. The bulk parameterization of Klemp and Wilhelmson (1978) was used.

The computational domain was assumed to be a subcloud ABL. The properties in the domain were supposed to be uniform in the horizontal, and hence the model configuration was 1D. At the top of the model domain, a rainwater content was prescribed steadily. No vertical air motion was assumed, and thus the evaporation of falling rain was focused on. Owing to the assumption of no air motion, weak intensity rains (1-10 $\mathrm{mm\,h^{-1}}$) were examined in the calculations. Strong intensity rains do not seem to be reasonable in the present 1D model because they are usually associated with strong vertical motions. Instead, some implications are obtained for strong intensity rains from the results of the present calculations.

3.1.1 Equations

The continuity equations of water vapor and rainwater (Kessler 1969) and the thermodynamic equation in the present model are given by:

$$\frac{\partial q_v}{\partial t} = E_r, \tag{3.1}$$

$$\frac{\partial q_r}{\partial t} = -\frac{1}{\rho}\frac{\partial}{\partial z}(\rho q_r V_t) - E_r, \tag{3.2}$$

$$\frac{\partial T}{\partial t} = -\frac{L_v}{C_p}E_r, \tag{3.3}$$

where E_r represents the rate of evaporation of rain, and V_t the terminal velocity of rainwater. E_r and V_t are given as follows (Klemp and Wilhelmson 1978):

$$E_r = \frac{1}{\rho}\frac{(1-q_v/q_{vs})C(\rho q_r)^{0.525}}{2.030\times10^4 + 9.584\times10^6/q_{vs}p}, \tag{3.4}$$

$$V_t = 36.34(0.001\rho q_r)^{0.1364}(\rho_0\sqrt{\rho})^{0.5}, \tag{3.5}$$

where q_{vs} is the saturation water vapor mixing ratio, $\rho_0 = 1.20\,\mathrm{kg\,m^{-3}}$, and C is the ventilation factor given by:

$$C = 1.6 + 30.3922(\rho q_r)^{0.2046} \tag{3.6}$$

All variables are in MKS units. The above equations were solved numerically with the vertical grid interval of 10 m and the time step of 1 s.

By assuming hydrostatic balance, atmospheric pressure was integrated vertically from the fixed pressure value at the top to model-level heights. Density temperature (T_ρ) defined by Emanuel (1994), which includes the weight of rainwater, was used for pressure calculation, and is given by:

$$T_\rho = T\frac{1+1.61q_v}{1+q_v+q_r}. \tag{3.7}$$

3.1.2 Initial and boundary conditions

Figure 3.1 shows mean thermodynamic vertical profiles at ZGY at 1200UTC on days when no precipitation was observed in August 1991. In Fig. 3.1, a nearly neutral profile of potential temperature is found in the lower levels up to around 4 km AGL. Thus, the top of the computational domain was assumed to be 4 km AGL. The profiles in the lowest 4 km in Fig. 3.1 were used as the initial condition. The initial ground pressure was assumed to be 850 hPa. At the top of the model domain, temperature, pressure, and relative humidity were set to remain constant throughout the time integration. Rainwater mixing ratio prescribed at the top of the model domain, q_{rtop}, was constant during time integration. Seven values of q_{rtop}, 0.08, 0.1, 0.2, 0.3, 0.4, 0.5, and $0.6\,\mathrm{g\,kg^{-1}}$, were examined. Figure 3.2 shows the relationship between the prescribed rainwater mixing ratio and rain intensity at the top of the model domain.

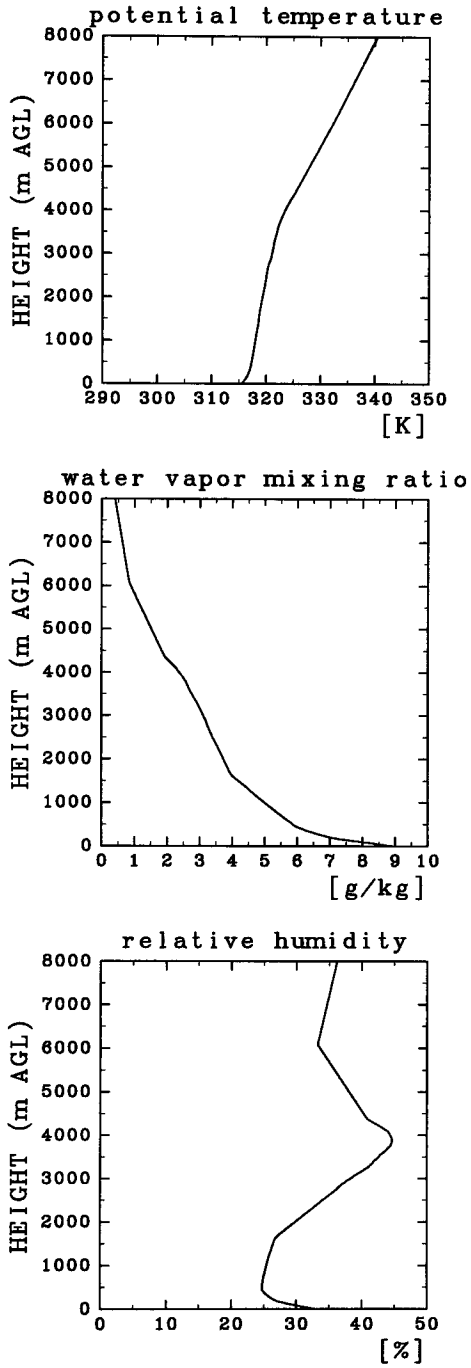

FIG. 3.1: The vertical profiles of mean potential temperature, water vapor mixing ratio, and relative humidity at ZGY at 1200 UTC in August 1991. No-precipitation days were chosen.

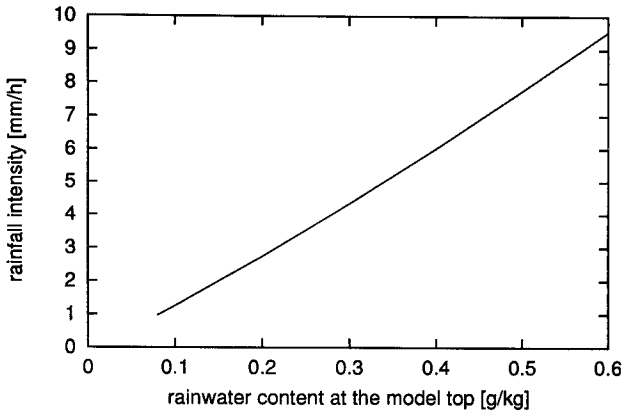

FIG. 3.2: The relationship between the rainwater mixing ratio ($g\,kg^{-1}$) and corresponding rain intensity ($mm\,h^{-1}$) at the model top.

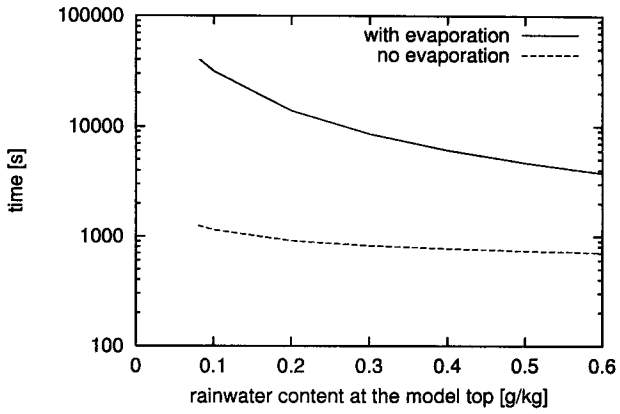

FIG. 3.3: The integration time when the total rainfall at the ground exceeds 0.1 mm, as a function of the rainwater mixing ratio at the model top. The solid line indicates calculations with evaporation, while the dashed line with no evaporation.

3.2 Results

Figure 3.3 shows the integration time when the accumulated rainfall at the ground exceeded 0.1 mm from the initial time as a function of rain intensity at the top of the domain. The calculation in which the evaporation of rain was set to zero ($E_r = 0$ in Eqs.(3.1)-(3.3)) is also shown for comparison. In Fig. 3.3, the time required for rain with $E_r \neq 0$ to reach the ground is much longer than that for rain with $E_r = 0$. This required time with $E_r \neq 0$ is longer than 11 h for a light intensity rain ($q_{rtop} = 0.08\,g\,kg^{-1}$: $0.97\,mm\,h^{-1}$), and is only about 1 h for a medium intensity rain ($q_{rtop} = 0.6\,g\,kg^{-1}$: $9.54\,mm\,h^{-1}$).

To show how much rain evaporates through the domain, the fraction of the accumulated evaporated rain at a level z to the accumulated rain at the model top was defined as (Rosenfeld and Mintz 1988):

$$F(z) = 1 - \frac{\text{accumulated rain at a level } z}{\text{accumulated rain at the top}}. \tag{3.8}$$

The result of the light rain intensity ($q_{rtop} = 0.08$) is shown in Fig. 3.4. This rain intensity corresponds to 23.3 mm day^{-1}; this value is almost the same with a rainfall event in the mountains area to the south of the HEIFE region (about 20 mm day^{-1}) in August 1991 (Sahashi 1995; Itano 1997). The strong dependence of F on height is seen (Fig. 3.4a). At the same time, moisture profile varies strongly with height (Fig. 3.4b). The surface rainfall does not occur even after 11 h (Figs. 3.4d, e). By 11 h the surface pressure rises more than 10 hPa (Fig. 3.4f). The total surface rainfall for 24 h is 11.0 mm, while the total rainfall given at the model top for 24 h is 23.2 mm. Thus, 53% of the total rain is depleted by evaporation before reaching the ground level. Furthermore, as seen in Fig. 3.4a, the F values at higher levels at $t = 24\,h$ greatly differ from that at the ground level. For instance, at the height of 1.5 km only

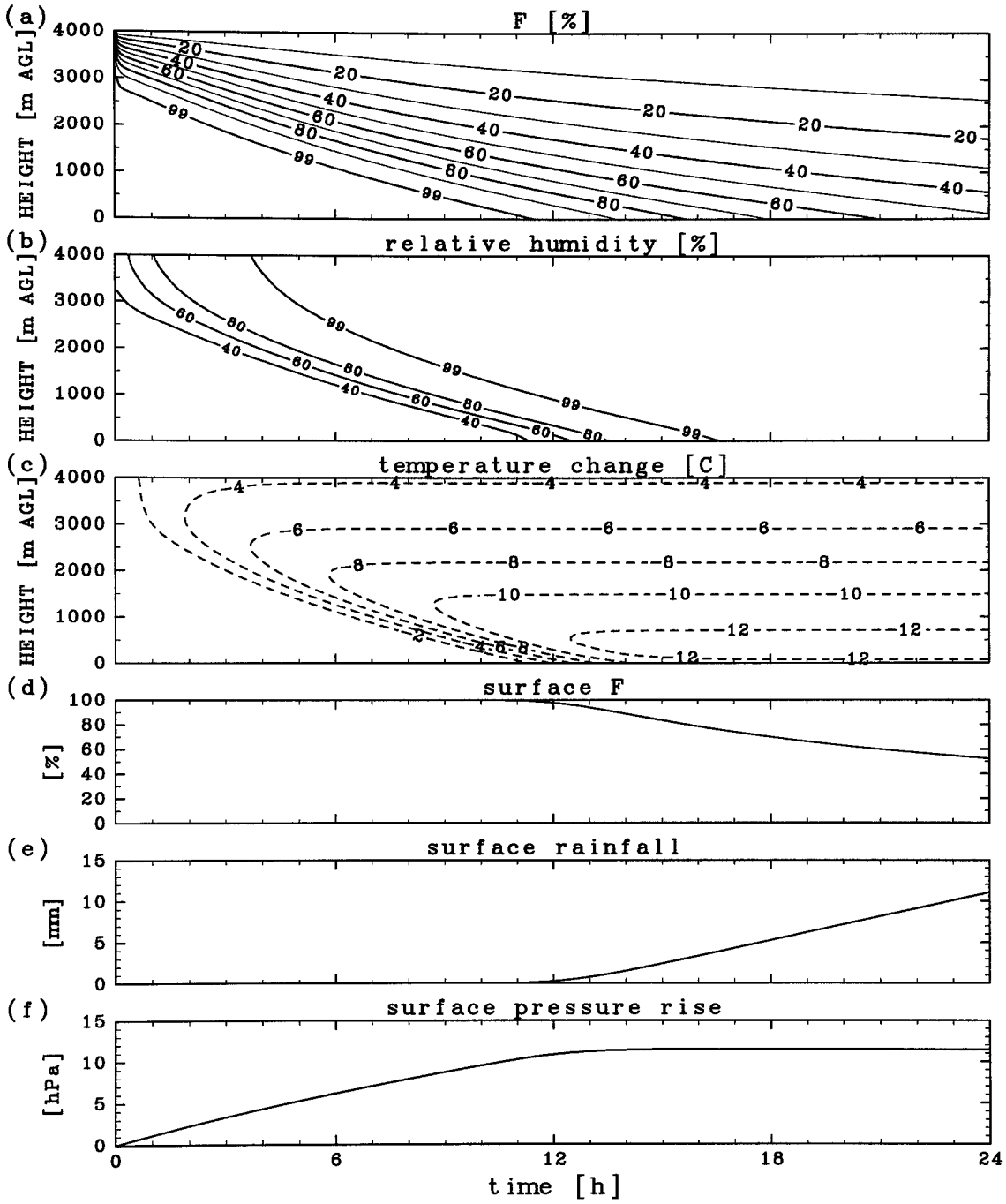

FIG. 3.4: Time series of (a) the fraction of total evaporated rain F, (b) relative humidity, (c) temperature drop, (d) surface F, (e) surface rainfall, and (f) surface pressure rise during 24 h when $q_{rtop} = 0.08\,\mathrm{g\,kg^{-1}}$ ($0.97\,\mathrm{mm\,h^{-1}}$). Isolines are drawn in the panels of the fraction of evaporated rain (the interval of 10% with an auxiliary isoline of 99%), relative humidity (the interval of 20% with an auxiliary isoline of 99%), and temperature drop (the interval of 2 K).

23% of the total rain is depleted. This height of 1.5 km was chosen because it corresponds to the elevation of the mountains relative to that of the desert.

In order to show the dependence of evaporated rain on rain intensity, a constant total amount of rain (20 mm) was provided at the top of the model domain for each rain intensity. Figure 3.5 shows the F value as a function of rain intensity. Although the same amount of total rain is provided at the top, F varies with rain intensity as well as height (Fig. 3.5a). At the ground level (Fig. 3.5b) F varies from 61 (the lightest rain: $0.97\,\mathrm{mm\,h^{-1}}$) to 68% (the heaviest rain: $9.54\,\mathrm{mm\,h^{-1}}$). As a result, the difference of surface rainfall between the heaviest and lightest intensity rain is about 1.5 mm (Fig. 3.5c). The amount of evaporated rain increases with rain intensity. This can be explained by the following reason: if rain intensity is strong, the rain falls faster and the ventilation factor defined in Eq.(3.6) becomes large; this large ventilation contributes to a large rate of rain evaporation and hence more depleted rain.

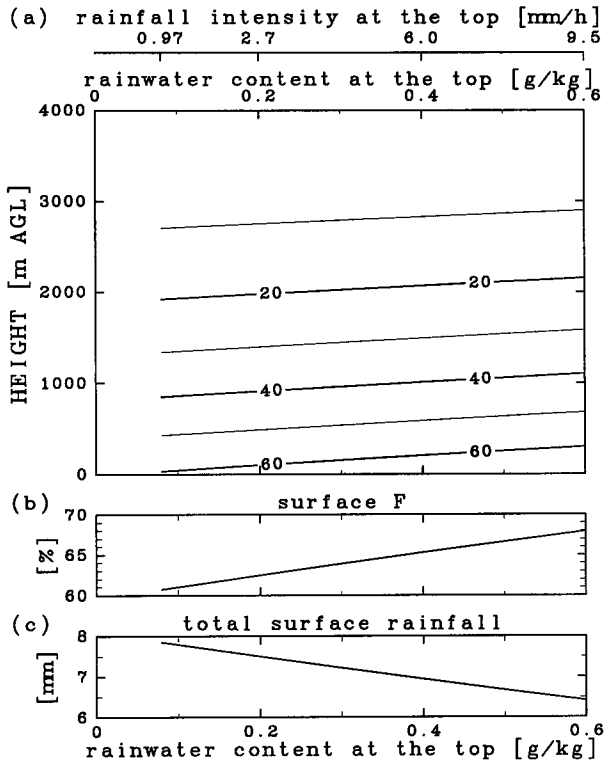

FIG. 3.5: (a) Height and rainfall intensity section of the fraction of evaporated rain F when a constant amount of total rain (20 mm) is provided at the model top for each q_{rtop}, (b) the surface F value, and (c) the surface total rainfall.

3.3 Remarks

The model results have shown that a heavier intensity rain evaporates faster than a lighter intensity rain (Fig. 3.5). From this result, in severe convective clouds over arid regions a large amount of rain is expected to evaporate in a subcloud layer. For the severe squall line on 5 May 1993, almost no rainfall was observed at the surface, while the surface relative humidity increased after the passage of this squall line, as described in chapter 2. In the pre-storm environment, a deep mixed layer developed, and its maximum depth was estimated as about 4.3 km. Thus, a significant amount of rain seems to evaporate before reaching the desert ground according to the calculations presented in this chapter.

For describing convective downdrafts, mixing of air in precipitating area with the ambient air should be taken into account. Thus, a more sophisticated 1D model may be appropriate in simulating realistically the evaporation of rain associated with downdrafts (Ogura and Takahashi 1971; Srivastava 1985). Mass conservation should be also taken into account (Kamburova and Ludlam 1966; Ryan and Carstens 1978; Leary 1980). Nevertheless, from the present results it is emphasized that the depth as well as the aridity of a subcloud layer strongly controls the rainfall in the desert region.

Chapter 4

Two-dimensional numerical experiments

4.1 Model description and experimental design

4.1.1 The numerical model

The model used here was a compressible, nonhydrostatic cloud model, the Advanced Regional Prediction System (ARPS, Xue et al. 1995). The computation was carried out under a two-dimensional configuration. The base-state environment was assumed constant in time and horizontally homogeneous. Surface friction and fluxes and Coriolis terms were neglected[1] The 1.5-order turbulent kinetic energy closure scheme, and the Lin et al. (1983) ice-phase microphysical schemes that represent six-category water substances (water vapor q_v, cloud water q_c, rainwater q_r, cloud ice q_i, snow q_s, and hail q_h) were adopted. The ARPS model employs the mode-splitting time integration scheme (Klemp and Wilhelmson 1978) that integrates acoustically active and inactive terms separately by two time steps. These two time steps were chosen to be 1 and 6 s here.

The model domain was 1800 km in the x direction (horizontal) and 18 km in the z direction (vertical). The vertical coordinate was height by AGL. The horizontal grid resolution was 1 km. The vertical resolution was 250 m from the ground to the 5-km level, and stretches from 250 m at the 5-km level to about 880 m at the top of the domain. The lower and upper boundaries were flat, rigid, and free slip. A Rayleigh-type damping layer existed above the 12-km level. The Orlanski (1976) radiation boundary condition was used for the lateral boundaries. The domain was translated at a constant speed ($17.5\,\mathrm{m\,s^{-1}}$) so as to keep the major convective disturbances away from the lateral boundaries. The wide horizontal domain was chosen for minimizing undesirable wave reflections from the lateral boundaries.

[1] See appendix A for the governing equations in our two-dimensional experiments.

4.1.2 Experimental design

The base state of the model was made from the morning sounding at Minqin as shown in Fig. 2.3 by assuming a ML in the low-level atmosphere. In chapter 2, the maximum ML depth at Minqin was estimated as about 4.3 km. Thus, the ML depth in the model was chosen to be 4375 m that was the height of the nearest grid point to the estimated ML height. Within this ML, the base-state profiles of potential temperature (θ) and water vapor mixing ratio (q_v) were defined so as to keep virtual potential temperature (θ_v) constant with height. The q_v profile was defined so as to keep the vertically integrated water vapor content within the assumed ML identical with that within the morning profile. q_v at the ML top was prescribed as $2.2\,\mathrm{g\,kg^{-1}}$ that corresponded to the relative humidity of 93%. q_v profile in the ML was assumed such that q_v decreased linearly with height. From the assumption of constant total moisture content within the ML, q_v at the surface was determined as $2.9\,\mathrm{g\,kg^{-1}}$ This surface q_v was about the same as the observed q_v in the afternoon on 5 May 1993. θ was calculated from q_v and the constant θ_v. The q_v and θ profiles thus obtained are shown in Figs. 4.1a, c. The experiment using these profiles is referred to as the control experiment (CNTRL).

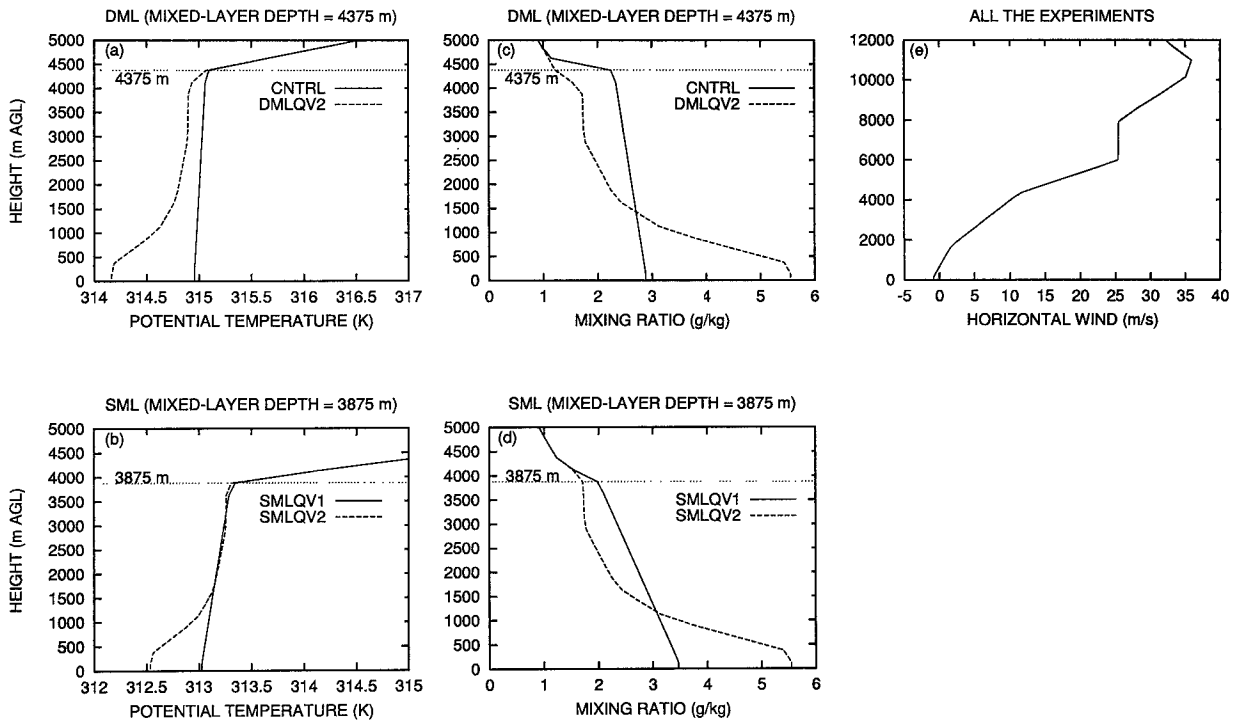

FIG. 4.1: Base-state profiles of low-level potential temperature for (a) experiments DML and (b) experiments SML, low-level water vapor mixing ratio for (c) experiments DML and (d) experiments SML, and (e) horizontal winds.

In addition to experiment CNTRL, sensitivity experiments were carried out. The morning q_v profile

was examined for investigating the sensitivity to low-level moisture profile. Furthermore, the sensitivity to ML depth was investigated by assuming another ML depth of 3875 m that was 500 m lower than the ML depth in CNTRL. Table 4.1 summarizes the numerical experiments. In SMLQV1, q_v at the ML top was prescribed as $2.0\,\mathrm{g\,kg^{-1}}$, and q_v in the ML was assumed to decrease linearly with height. Experiment SMLQV1 was chosen because the CAPE value in this experiment was nearly the same as that in CNTRL. The low-level profiles of θ and q_v for the sensitivity experiments are shown in Figs. 4.1a-d. For all the experiments, the observed profile of horizontal winds was used. The base-state winds in the model were defined by subtracting $17.5\,\mathrm{m\,s^{-1}}$ from the winds shown in Fig. 4.1e. The initial surface pressure was set to be 850 hPa.

Convection was initiated by placing an ellipsoidal warm thermal (maximum potential temperature excess 3 K) having a horizontal radius of 10 km and a vertical radius of 3 km. This thermal was centered at $(x, z) = (550\,\mathrm{km}, 0\,\mathrm{km})$.

TABLE 4.1: List of experiments. In the column of moisture profile, "Linear" means water vapor mixing ratio (q_v) decreases linearly with height within the ML, and "morning" means the morning profile at Minqin. The thermodynamic variables are for a surface air parcel.

Experiment	ML depth (m)	Moisture profile	q_v ($\mathrm{g\,kg^{-1}}$)	Relative humidity (%)	CAPE ($\mathrm{J\,kg^{-1}}$)	LCL (m)	LFC (m)
CNTRL	4375	Linear	2.9	11	250	4090	4140
DMLQV2	4375	Morning	5.6	22	1230	2950	3150
SMLQV1	3875	Linear	3.5	15	240	3580	3680
SMLQV2	3875	Morning	5.6	24	1090	2770	2940

4.2 The control experiment

4.2.1 Squall-line evolution and structure

Figure 4.2 shows the time-space diagrams of potential temperature perturbation (θ') at the surface, updraft velocity at the 4-km level, and vertical velocity at the 6-km level. In Fig. 4.2a, a surface cold pool becomes significant ($\theta' < -10\,\mathrm{K}$) after 9 h, and has a wide horizontal area after 10 h. After 10 h, the system is referred to as in its mature stage. The surface cold pool did not decay until the end of time integration (15 h). At the 4-km level (Fig. 4.2a), a strong updraft of greater than $4\,\mathrm{m\,s^{-1}}$ persists at the leading edge of the cold pool. Also at the 6-km level (Fig. 4.2b), an updraft sustained.

The vertical structure of the squall line at 10, 10.5, and 11 h is shown in Fig. 4.3. The leading edge of the cold pool is defined as the position where θ' is $-1\,\mathrm{K}$ at the surface. At 10 h (Fig. 4.3a), there are two

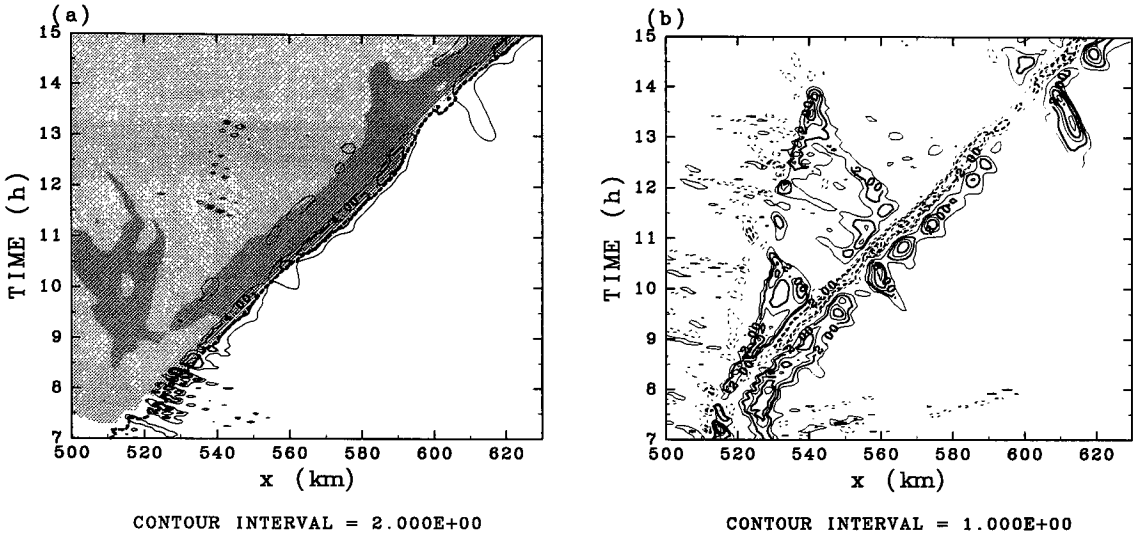

FIG. 4.2: Horizontal-time section of (a) potential temperature perturbation (θ', shaded) at the surface and updraft velocity (contoured) at the 4-km level and (b) vertical velocity at the 6-km level for CNTRL. Lighter shaded indicates θ' between -10 and -3 K, and darker shaded θ' of less than -10 K. Contour intervals are $2\,\mathrm{m\,s^{-1}}$ in (a) and $1\,\mathrm{m\,s^{-1}}$ in (b). The thick dotted line is θ' of -1 K contour.

main updrafts on the both front and rear side of the leading edge of the cold pool: at $x = 8$ and 0 km on the front side; and at $x = -16$ and -25 km on the rear side. At 10.5 h the updraft at the cold pool edge combines with the another updraft ahead of the cold pool to form a deep updraft penetrating into the upper troposphere (Fig. 4.3b). On the other hand, the two updraft regions behind the cold pool edge seen at 10 h temporally strengthen and weaken: at 10.5 h the updraft branch located at 30 km behind the cold pool edge strengthens (Fig. 4.3b); and at 11 h the updraft located at 16 km behind the cold pool edge strengthens (Fig. 4.3c). The intensification of these updrafts is associated with the positively buoyant air in the mid-levels at around $x = -12$ km. As the updraft branch in the rear side of the cold pool edge translates rearward, the cloud region simultaneously expands rearward. In Fig. 4.3, a strong downdraft is found just behind the cold pool edge at around $x = -8$ km.

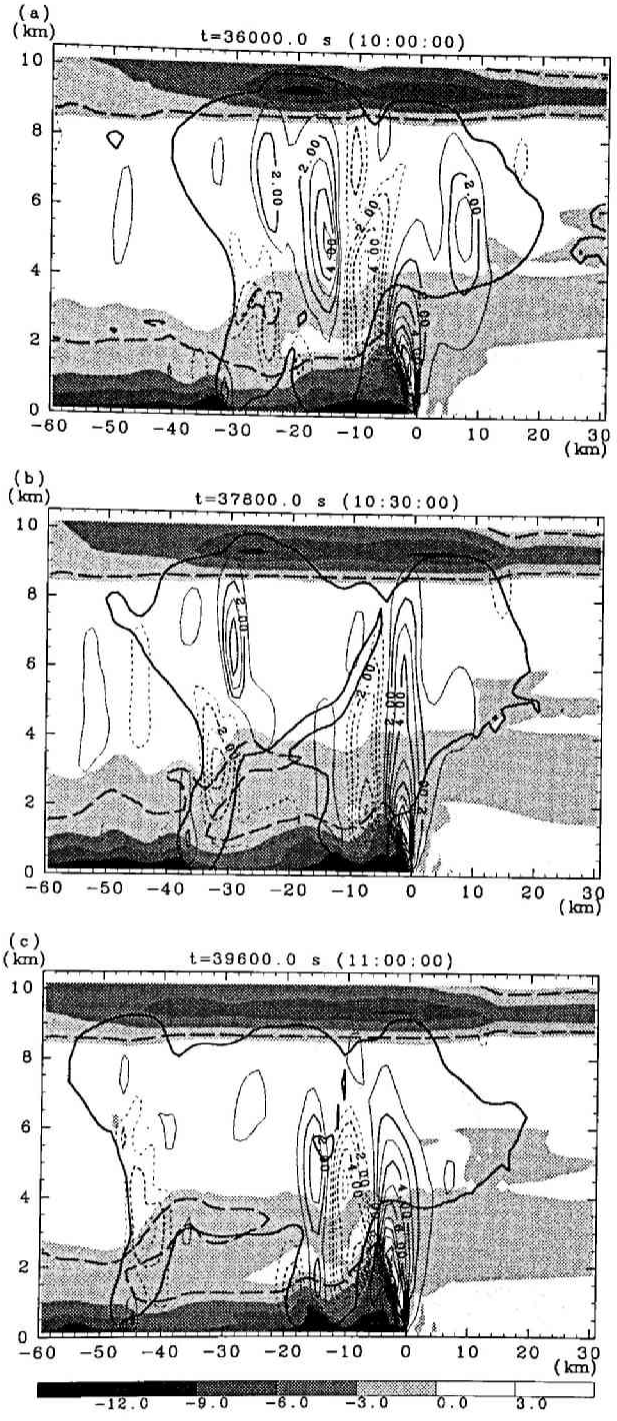

FIG. 4.3: Vertical cross sections of the squall line in CNTRL at $t = 10$, 10.5, and 11 h. Vertical velocity (contoured, every $1\,\mathrm{m\,s^{-1}}$), θ' (shaded, the interval of 2 K), and total condensate mixing ratio ($0.1\,\mathrm{g\,kg^{-1}}$, heavy contour lines) are shown. $\theta' = -1\,\mathrm{K}$ is contoured by the dashed lines. The horizontal coordinate is indicated by a storm-relative sense such that the leading edge of the cold pool is at $x = 0\,\mathrm{km}$.

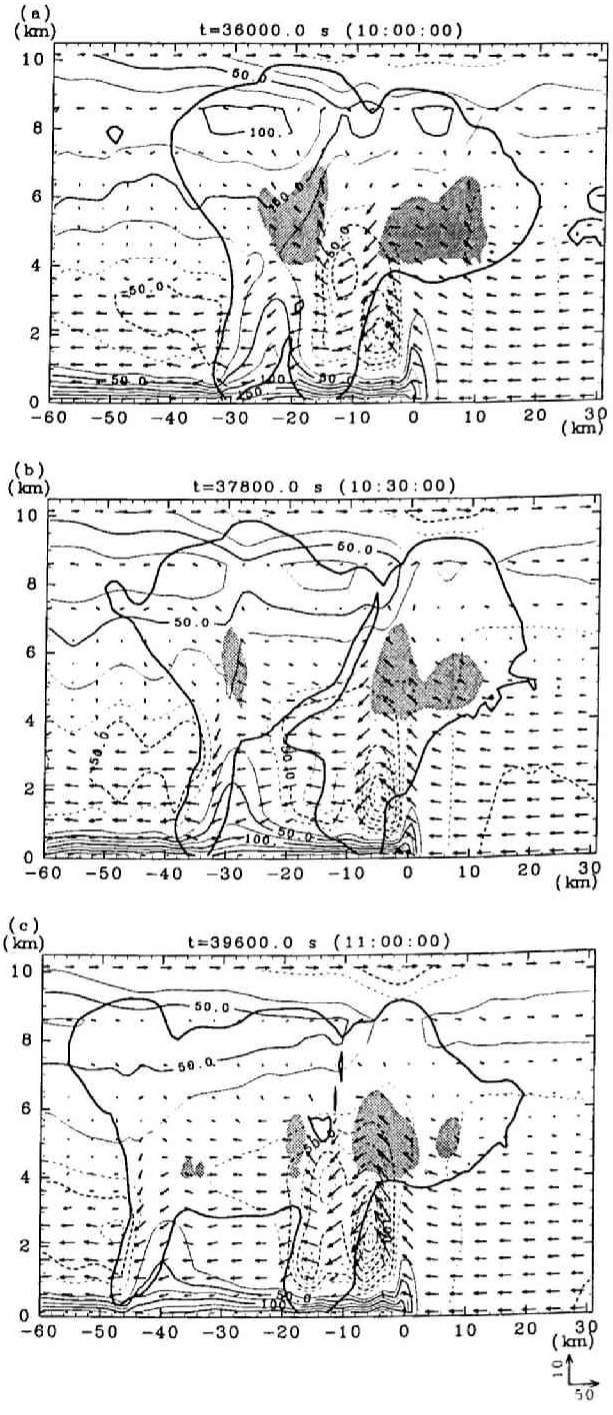

FIG. 4.4: Same as Fig. 4.3 except for pressure perturbation (contoured every 25 Pa), system-relative wind field (the unit vector is indicated in the lower right corner, $\mathrm{m\,s^{-1}}$), and cloud water field (shaded, $q_c > 0.05\,\mathrm{g\,kg^{-1}}$.)

Figure 4.4 shows the vertical cross sections of the system-relative wind, pressure perturbation, and cloud water fields at the same times with Fig. 4.3. In Fig. 4.4, the system-relative flow just above the cold pool is generally front-to-rear, accelerated by the rearward horizontal pressure gradient force associated with a strong low pressure at about 2 km AGL just behind the leading edge of the cold pool. This low is hydrostatically induced by the positive buoyant air located above as shown in Fig. 4.3. In Fig. 4.4, a small-scale high pressure perturbation exists just ahead of the cold pool. The cloud water is produced just above the height of the ML top. The maximum q_c during 10-11 h is $0.42\,\mathrm{g\,kg^{-1}}$ Above the 5-km level, q_s dominates the condensate fields, with its maximum value during 10-11 h being $2.2\,\mathrm{g\,kg^{-1}}$

Diabatic cooling induced by microphysical processes was examined here. Figure 4.5 shows four diabatic cooling fields. In this figure, the evaporation of rain (Fig. 4.5d) is dominant in the lower part of the ML. Above the 3-km level, the sublimation of snow and hail (Figs. 4.5b,c) dominates the cooling field. Because of the evaporation and sublimation of precipitation, the surface rainfall occurred only during t = 7-11 h, and the maximum accumulated rainfall during the period of 10-12 h was only 0.8 mm.

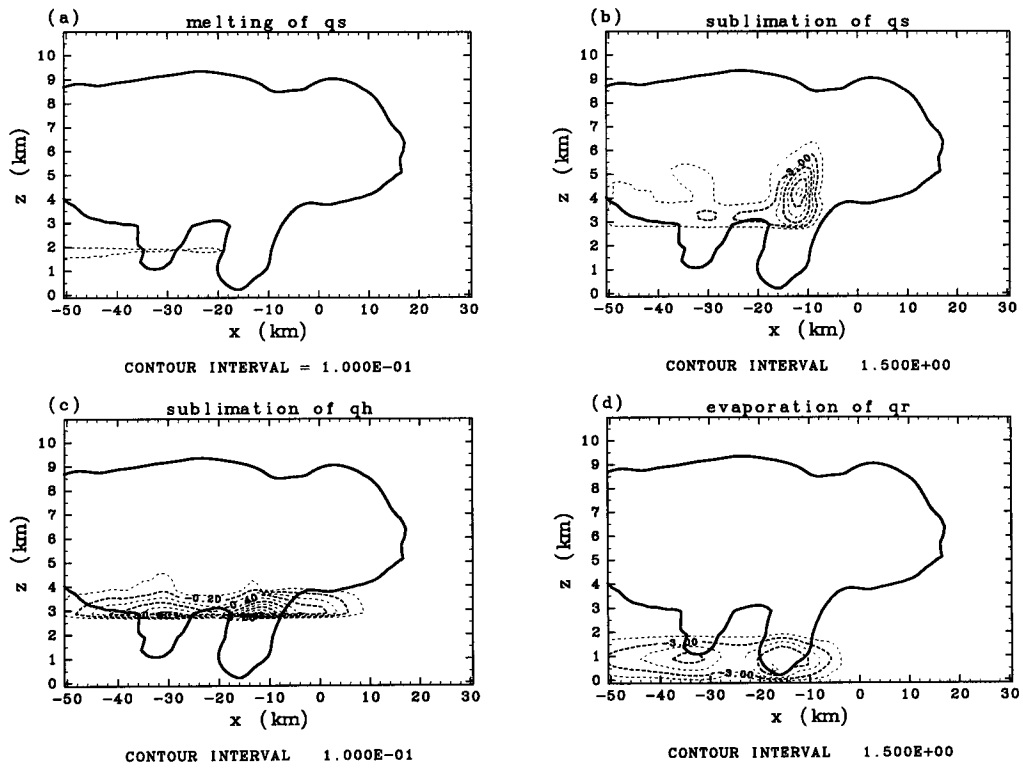

FIG. 4.5: Diabatic cooling ($\mathrm{K\,h^{-1}}$) fields averaged during 10-12 h for CNTRL. (a) Melting of snow, (b) sublimation of snow, (c) sublimation of hail, (d) evaporation of rain. The contour intervals are $0.1\,\mathrm{K\,h^{-1}}$ in (a) and (c), and $1.5\,\mathrm{K\,h^{-1}}$ in (b) and (d). Total condensate mixing ratio of $0.1\,\mathrm{g\,kg^{-1}}$ from the 2-h-averaged field is contoured by the heavy line.

4.2.2 Air parcel trajectories

Air parcel trajectories were calculated by the method of Doty and Perkey (1993) by using the wind fields at every time step. The air parcels were initially placed at 10 h, and their trajectories were integrated for the subsequent 2 hours.

Figure 4.6a and b show the trajectories of air parcels originating ahead of and behind the leading edge of the cold pool, respectively, during the mature stage (10-12 h). In Fig. 4.6a, the air parcels originating between 125-2375 m level (bellow the originating height of trajectory C) slightly go up near the leading edge of the cold pool and sink behind the cold pool edge at around $x = -20\,\mathrm{km}$. On the other hand, air parcels originating above the 2675-m level go up to the upper troposphere. Among these upward-moving parcels, there are two patterns of trajectories: trajectories A and B. The required times to reach the maximum heights for trajectories A and B are 6300 and 1500 s, respectively.

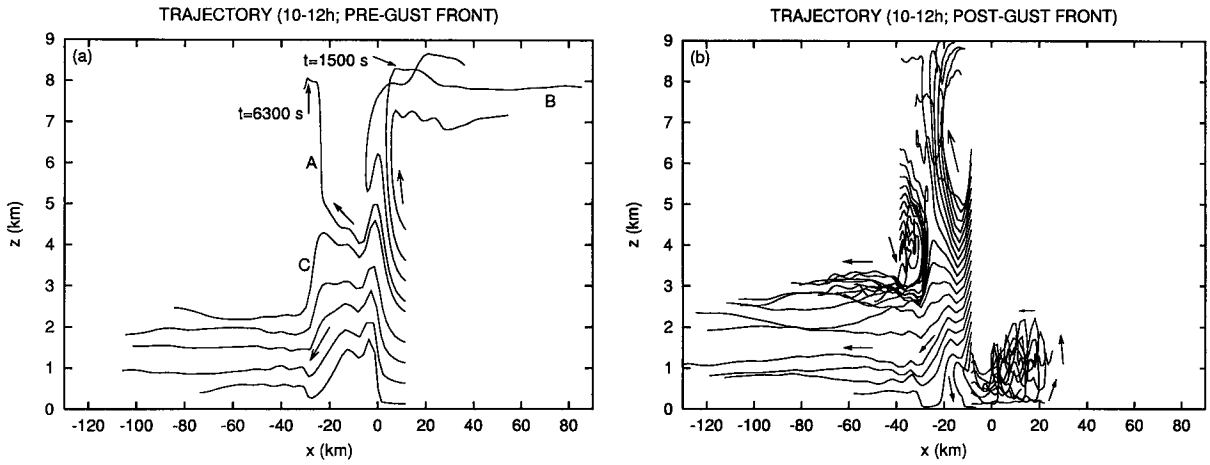

FIG. 4.6: Air parcel trajectories during 10-12 h for CNTRL. (a) The origins of parcels are at $x = 10\,\mathrm{km}$. Arrows with characters indicating times point to the required times to reach the maximum heights for trajectories A and B. (b) The origins of parcels are at $x = -40\,\mathrm{km}$ between $z = 3625\,\mathrm{m}$ and $6363\,\mathrm{m}$, and at $x = -10\,\mathrm{km}$.

In Fig. 4.6a, the parcels reaching the upper troposphere originate in the upper part of the ML. The paths of these parcels contrast with the airflow in the typical squall line systems in midlatitude and tropical regions: the low-level potentially unstable air is transported upward and feeds convective clouds. Tracer analysis described later will also show the similar character of the airflow in CNTRL.

The downward motion along trajectory C in Fig. 4.6a seems to be similar to an up-down branch of low-level downdrafts. Knupp (1987) found that the up-down downdraft originates within the ABL and emerges during mature convective storms over the High Plains. This type of downdraft branch was also found in an observed squall line over the High Plains, and contributed primarily to the maintenance of the subcloud cold pool through precipitation evaporation (Fankhauser et al. 1992).

In Fig. 4.6b, the parcels originating at $x = -10\,\mathrm{km}$ above $z = 4375\,\mathrm{m}$ go up to the upper troposphere. On the other hand, the parcels originating at $x = -10\,\mathrm{km}$ bellow $z = 4125\,\mathrm{m}$ go downward: the parcels originating bellow $z = 1875\,\mathrm{m}$ are transported into a cold pool region; and the others are advected rearward. As shown in Fig. 4.5, evaporation of rain contributed to the boundary-layer cooling to produce the cold pool. The parcels entering the cold pool originally come from the pre-storm dry ML. Thus, the dry low-level air ahead of the cold pool contributes to the enhancement of rain evaporation.

The parcels originating at $x = -40\,\mathrm{km}$ between $z = 3625\,\mathrm{m}$ and $6363\,\mathrm{m}$ slowly go forward as they go downward (Fig. 4.6b). The speeds of these forward movements, however, are slower than that of the cold pool. These parcels are then advected rearward and do not go down to near the ground. Thus, the mid-level air in the rear of the system is not likely to contribute the intensification of the cold pool.

Consequently, the surface cold-air pool is primarily fed by the dry low-level inflow from ahead of the pool. The role of this low-level inflow was different from the fact shown by Zipser (1977) that the transient dry mid-level inflow from ahead of a squall line down into a cold pool region contributes to the boundary layer cooling. It was also different from the fact that dry rear inflow jet in a squall line contributes to the strength of the cold pool (Smull and Houze 1987; Fovell and Ogura 1989).

4.2.3 Forcing of vertical velocity acceleration

To show the dynamics involved in the updraft and downdraft originating in the ML, the vertical accelerations along air parcel trajectories were examined by using the vertical momentum equation

$$\underbrace{\frac{Dw}{Dt}}_{\mathrm{PWDT}} = \underbrace{-\frac{1}{\bar{\rho}}\frac{\partial p'}{\partial z}}_{\mathrm{VPGA}} + \underbrace{g\left(\frac{\theta'}{\bar{\theta}} + 0.61 q_v'\right) - \underbrace{g(q_c + q_r + q_i + q_s + q_h)}_{\mathrm{LOAD}}}_{\mathrm{BUOY}}. \tag{4.1}$$

Turbulent mixing term was neglected here. The overbar denotes the base-state variables, and the prime the perturbation variables. As shown in (4.1), the parcel vertical velocity acceleration (PWDT) was decomposed into two parts: the vertical pressure gradient (VPGA) and total buoyancy including condensate loading (BUOY). The contribution of condensate loading to buoyancy (LOAD) was also calculated. Figure 4.7 shows the spatial distribution of the four terms indicated in (4.1) at 10 h.

Figures 4.8 and 4.9 show the forcings of vertical acceleration in (4.1) along trajectories A and B, respectively, before the parcels reach their maximum levels. The parcels along trajectories A and B are first accelerated upward by VPGA. After the initial acceleration by VPGA, the air parcels along the two trajectories experience slightly different patterns of the forcings with each other. In Fig. 4.8b, as the parcel along trajectory A is advected rearward, it experiences a strong negative VPGA ($t = 1000$-1500 s). Because the magnitude of this negative VPGA is greater than that of positive BUOY, the air parcel is accelerated downward. Thus, the vertical velocity becomes negative (Fig. 4.8a). After 1500 s, the parcel along trajectory A is accelerated upward by a positive BUOY, reaching the upper troposphere.

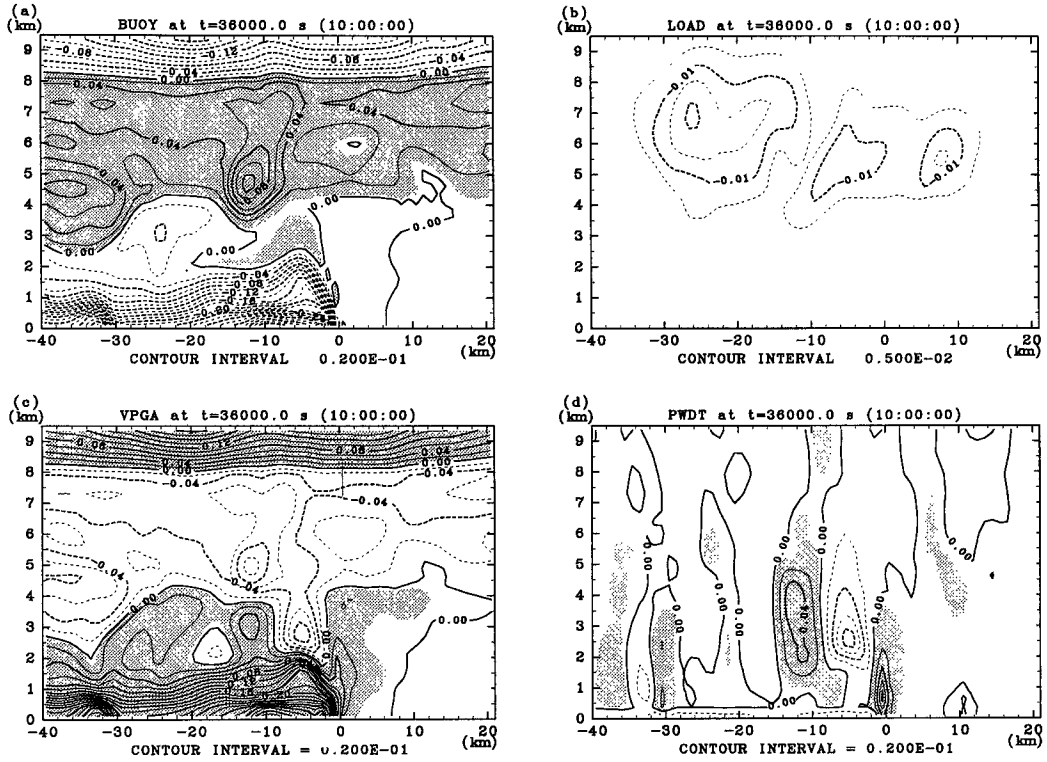

FIG. 4.7: Fields of vertical velocity acceleration, (a) BUOY, (b) LOAD, (c) VPGA, and (d) PWDT, at $t = 10\,\mathrm{h}$ in CNTRL. The values greater than $0.005\,\mathrm{m\,s^{-2}}$ are shaded.

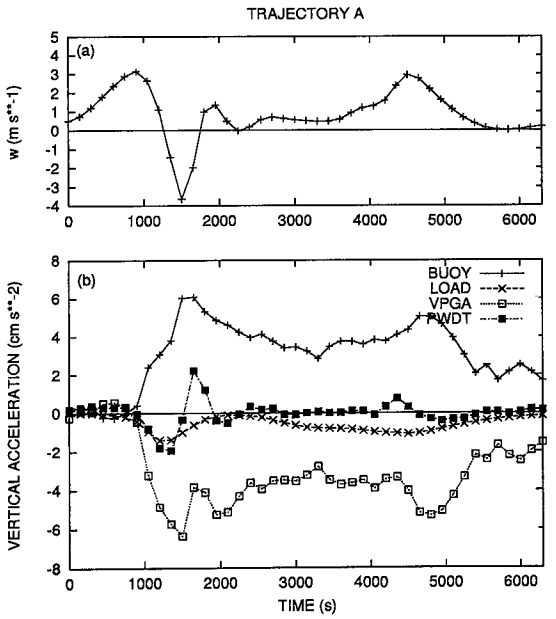

FIG. 4.8: Time sequences of (a) the vertical velocity and (b) BUOY, LOAD, VPGA, and PWDT as indicated in (4.1) along trajectory A in CNTRL.

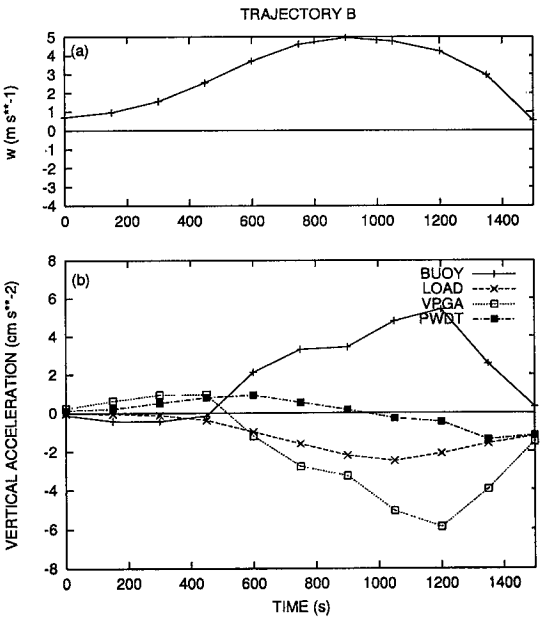

FIG. 4.9: Same as Fig. 4.8 except for trajectory B.

On the other hand, the air parcel along trajectory B also experiences negative VPGA, but the magnitude of this negative VPGA is smaller than that of positive BUOY (Fig. 4.9b, t = 600-900 s). Thus, the parcel is accelerated upward and achieves the maximum updraft velocity at 900 s (Fig. 4.9a). Although the parcel goes up in the precipitation zone of the forward extending anvil, the magnitude of LOAD is not large. Thus, the parcel does not substantially experience a detrimental effect of condensate loading.

For the downdraft, the air parcel along trajectory C initially went up slightly by positive VPGA, but soon experienced strong negative VPGA. After exiting the strong negative VPGA region, however, BUOY was not so large. Thus, the parcel was not transported upward. The downward acceleration within this downdraft was mainly provided by negative vertical pressure gradient force.

4.3 The sensitivity experiments

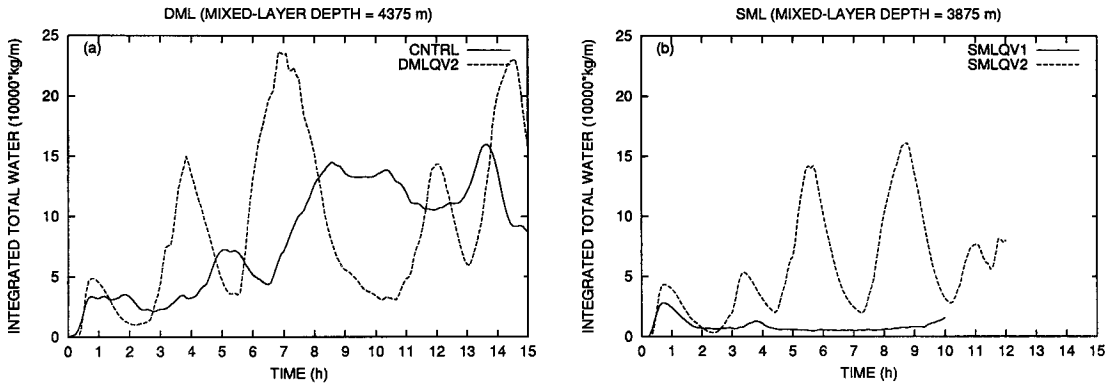

FIG. 4.10: Time series of domain-integrated total liquid and ice water content for (a) experiment DML and (b) experiment SML.

Figure 4.10 shows the time series of domain-integrated total liquid and ice water contents, Σq_w. In this figure, the evolution largely differs among the experiments. The evolution of the squall lines in the sensitivity experiments is described in the following.

4.3.1 Sensitivity to low-level moisture profile

In experiment DMLQV2, there are peak values of Σq_w at around 4, 7, 12, and 14.5 h after the initial thermal decays (Fig. 4.10a). The maximum value of Σq_w at about 7 h in DMLQV2 is larger than that in CNTRL, but at around 10-11 h the value of Σq_w becomes much smaller.

The evolution of the squall line in DMLQV2 can be found in the evolution of a surface cold pool and updraft velocity at the 4-km level (see Fig. 13 of TS98). The cold pool strengthens ($\theta' < -10$ K) and occupies a wide horizontal extent after 7.5h. After 8 h the squall line in DMLQV2 is referred to as in its mature stage. The cold pool advances over the subsequent 2 hours, but it gradually decays after 10 h.

Figures 4.11 and 4.12 show the evolution of the squall-line structure in DMLQV2. In Figs. 4.11a and 4.12a, the overall structure is similar to that in CNTRL. A feature distinguished from CNTRL is that the updraft at the leading edge of the cold pool does not reach the upper troposphere. After 9 h, the system soon begins to lose its organized structure (Figs. 4.11b and 4.12b). Although cloud water is persistently present at $x = 0$ km just above the ML top over the period shown in Fig. 4.12, the cloud region in the rear of the system begins to disappear at 9 h.

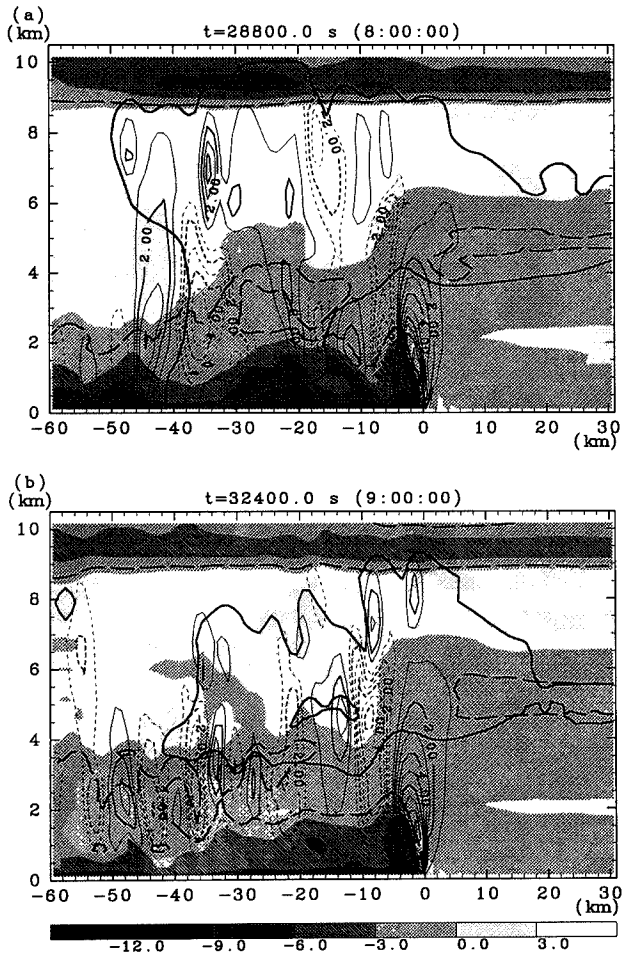

FIG. 4.11: Same as Fig. 4.3 except for experiment DMLQV2 at $t = 8$ and 9 h.

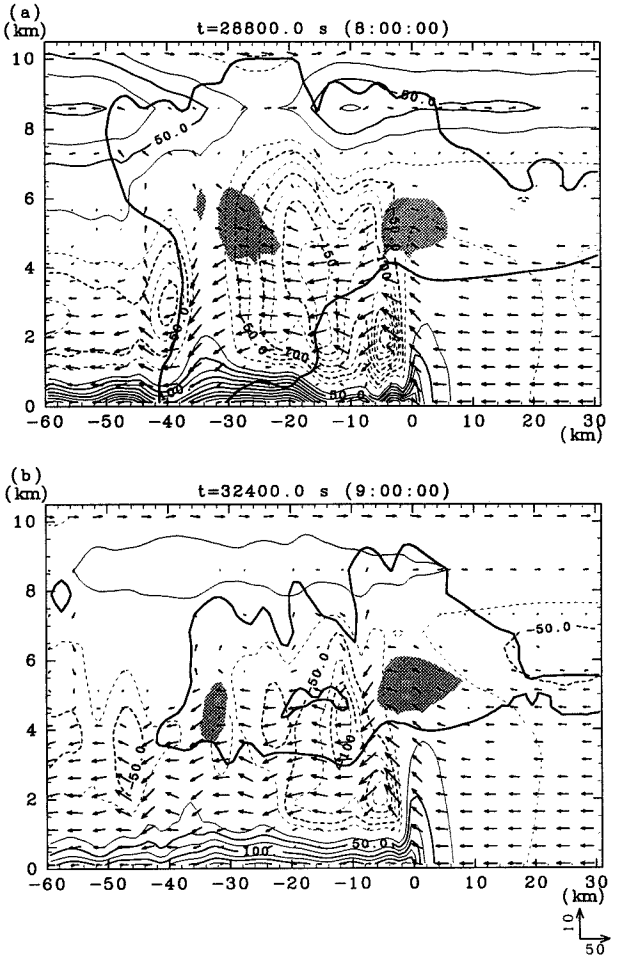

FIG. 4.12: Same as Fig. 4.4 except for experiment DMLQV2 at $t = 8$ and 9 h.

To show the different evolution between the mature squall lines in CNTRL and DMLQV2, the transport of air originating in the ML ahead of the cold pool was investigated by placing passive tracers into the two layers within the ML ahead of the cold pool in the mature stages for CNTRL and DMLQV2. Tracer 1 was initially placed into the lower ML between 0-2 km AGL, and tracer 2 into the upper ML between 2-4.5 km AGL. The concentrations of these tracers were initialized to unity in each layer, but were elsewhere zero. These tracers were initially placed at $t = 10$ h for CNTRL, and at $t = 8$ h for DMLQV2.

Figure 4.13 shows the tracer 1 fields after 2 h of simulations. For the both experiments, tracer 1 is not transported upward. Instead, this tracer is transported mainly to the rear of the system and partly into the cold pool region.

The tracer 2 fields between CNTRL and DMLQV2 are quite different, in contrast to the tracer 1 fields. In Fig. 4.14a, tracer 2 for CNTRL enters updraft regions and is transported upward to the upper troposphere. High tracer concentration (>80%) is found within the layers of mid-to-upper troposphere, showing the high efficiency of upward transport of the ML air. On the contrary, tracer 2 for DMLQV2 is not transported upward but is transported rearward (Fig. 4.14b). Owing to the absence of the upward transport, the squall line in DMLQV2 soon weakened after the cold pool achieves its mature state.

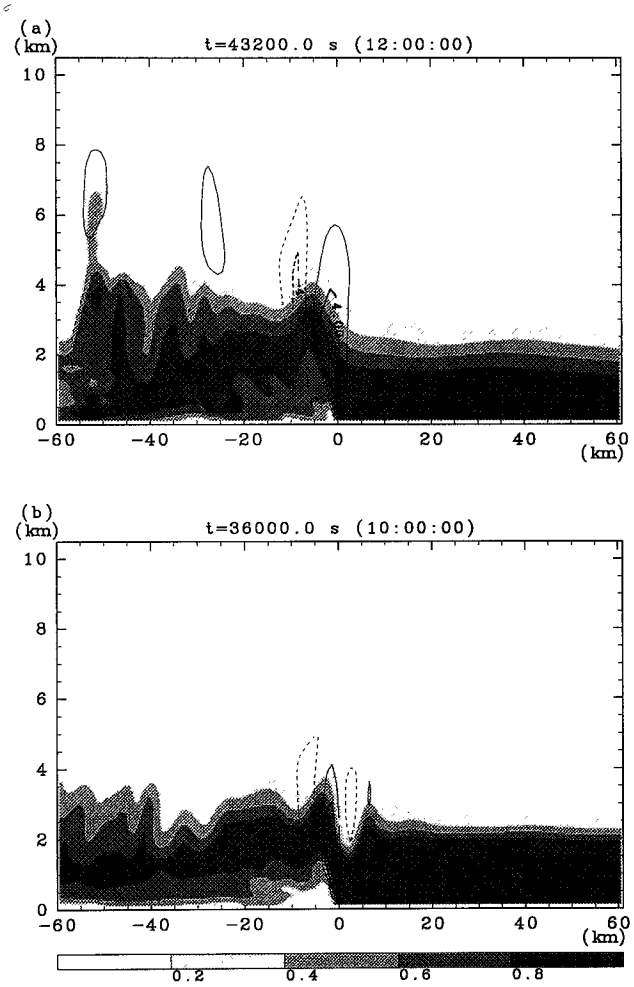

FIG. 4.13: Tracer 1 fields (shaded) after 2 h of simulation at (a) $t = 12\,\mathrm{h}$ for CNTRL and (b) $t = 10\,\mathrm{h}$ for DMLQV2. Vertical velocity field is also shown ($2\,\mathrm{m\,s^{-1}}$ contours).

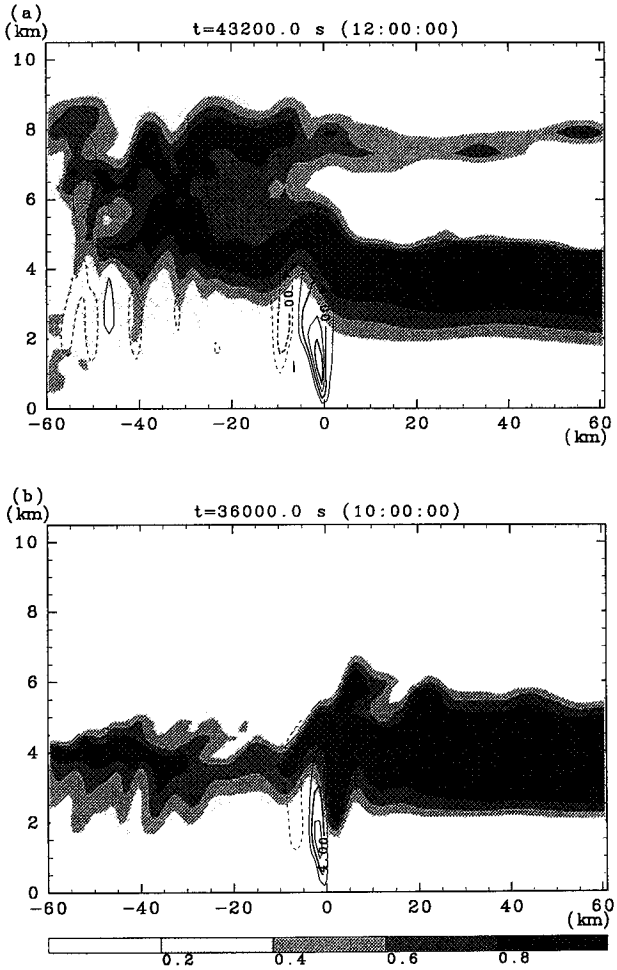

FIG. 4.14: Same as Fig. 4.13 except for tracer 2.

4.3.2 Sensitivity to mixed-layer depth

In Fig. 4.10b, the value of Σq_w in SMLQV2 has some peaks after the initial development during the first 1 h. On the contrary, in SMLQV1 the value of Σq_w does not re-increase, though the surface CAPE in SMLQV1 is similar to that in CNTRL (see Table 4.1).

The results of SMLQV2 were compared with those of CNTRL and DMLQV2 to show the effects of mixed-layer depth on squall-line evolution. Figure 4.15 shows the evolution of a surface cold pool and updraft velocity at the 4-km level. Updrafts begin to intensify at 7.5 h. A strong cold pool ($\theta' < -10\,\mathrm{K}$) is found during 9-9.5 h. During this period the updraft at the cold pool edge, however, is very weak, and the cold pool soon weakens. The updraft and surface cold pool in SMLQV2 sustain for a shorter period than those in DMLQV2 and CNTRL. Although the CAPE in SMLQV2 is much larger than that in CNTRL and is comparable with that in DMLQV2, the period between the intensification and weakening of the surface cold pool and Σq_w in SMLQV2 is shorter than those in CNTRL and DMLQV2.

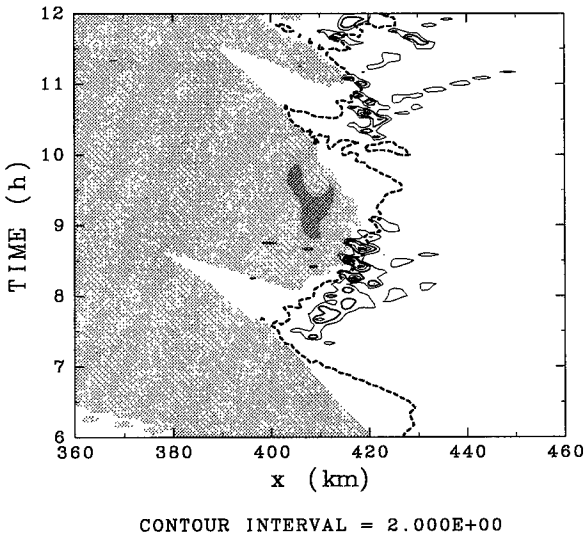

FIG. 4.15: Same as Fig. 4.2a except for experiment SMLQV2 during 6-12 h.

In addition to the above experiments, an experiment with the ML depth of 3375 m and morning q_v profile was also carried out. Although the CAPE for the surface parcel in this experiment was $913\,\mathrm{J\,kg^{-1}}$, convection was not sustained after the initial thermal decayed (not shown). Therefore, the presence of a deep ML is a necessary condition for the long-lived squall lines in dry environments.

4.4 Release of CAPE and maintenance mechanism of the squall lines

Figure 4.16 shows the CAPE and the difference between the LFC and parcel source level as a function of the source level of a parcel in the ML. The calculations of CAPE and LFC were based on the base-state variables. At the surface, the CAPE values in DMLQV2 and SMLQV2 are much larger than those in CNTRL and SMLQV1. As the parcel source level increases, the CAPE sharply decreases, and the difference between the LFC and the parcel source level increases in DMLQV2, SMLQV1, and SMLQV2. In these three experiments, the CAPE values of the parcels originating in the upper part of the ML are zero. On the other hand, in CNTRL the CAPE values of the parcels originating at levels above $z = 2.5\,\mathrm{km}$ are still in the range of 50-150 $\mathrm{J\,kg^{-1}}$, and the differences between the LFCs and parcel source levels are less than 1.5 km. For instance, the parcel originating at $z = 3625\,\mathrm{m}$, which will go along trajectory B during 10-12 h in CNTRL (Fig. 4.6a), has to be lifted only 831 m to reach its LFC. As a result, the parcels originating at the upper levels of the ML can be easily lifted to their LFCs. In contrast to these upper parcels, low-level parcels are difficult to be lifted because the differences between the LFCs and parcel source levels are large.

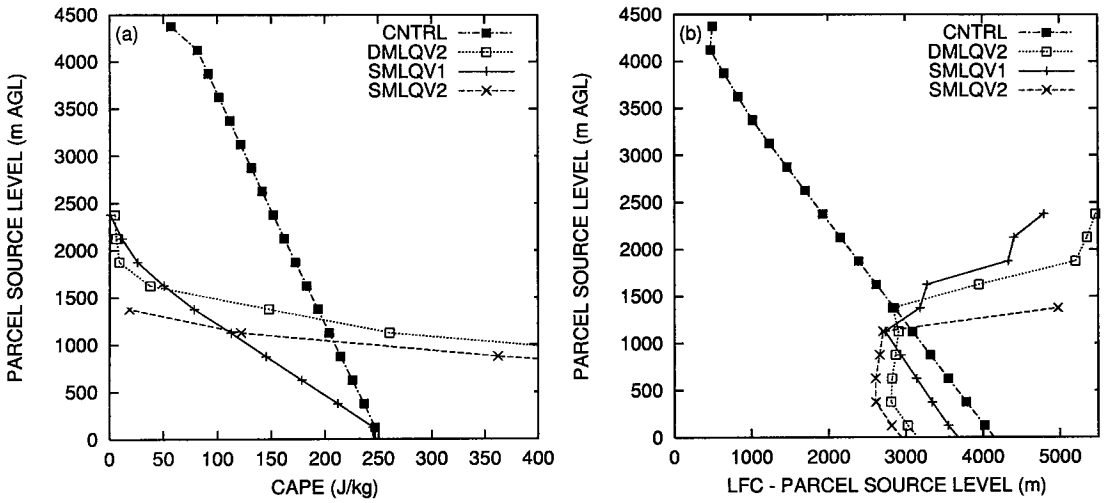

FIG. 4.16: (a) CAPE and (b) the difference of height between the LFC and parcel source level for the parcels originating in the ML as a function of the source levels of the parcels. The calculations were based on the base-state variables.

The work required to lift an air parcel to its LFC, the convective inhibition (CIN), is represented as a barrier to the initiation of convection. CIN is defined as the net work per unit mass required to lift a negatively buoyant air parcel from the source level i to the LFC, and is given by (Colby 1984; Bluestein

and Jain 1985)

$$\mathrm{CIN} = -\int_i^{\mathrm{LFC}} g\left(\frac{\theta_{vp} - \theta_{va}}{\theta_{va}}\right) dz, \tag{4.2}$$

where θ_{vp} and θ_{va} are the virtual potential temperatures of an air parcel and the ambient, respectively. Crook (1996) showed that convection initiation depends very sensitively on the magnitude of CIN. It should be noted that in the present situation where θ_v within the ML was constant, CIN was virtually zero for the parcels in the lower part of the ML. No forcing seems to be required to lift these parcels to their LFCs. Thus, the CAPE for these parcels appears to be easily released. However, persistent convection was not always produced in all the experiments. Alternative factors, therefore, must control the inhibition of convection. Mixing process and length of parcel trajectory can play a role in controlling the release of CAPE, as Weisman (1992) and Williams and Renno (1993) suggested.

In the present experiments, turbulent mixing of momentum can be important. The turbulent mixing term in the vertical momentum equation is calculated by the following formulation:

$$K_m\left(\frac{\partial^2 w}{\partial x^2} + \frac{\partial^2 w}{\partial z^2}\right), \tag{4.3}$$

where K_m is the turbulent mixing coefficient for momentum.

Figure 4.17 shows the turbulent mixing term at 10 h in CNTRL and at 8 h in DMLQV2. Negative effects of this mixing are found near the cold pool's boundary. Thus, the parcel traversing along the cold pool's boundary will experience the deceleration by this turbulent mixing, entrained into the cold pool region. This entrainment can be found in the tracer analysis as shown in Fig. 4.13.

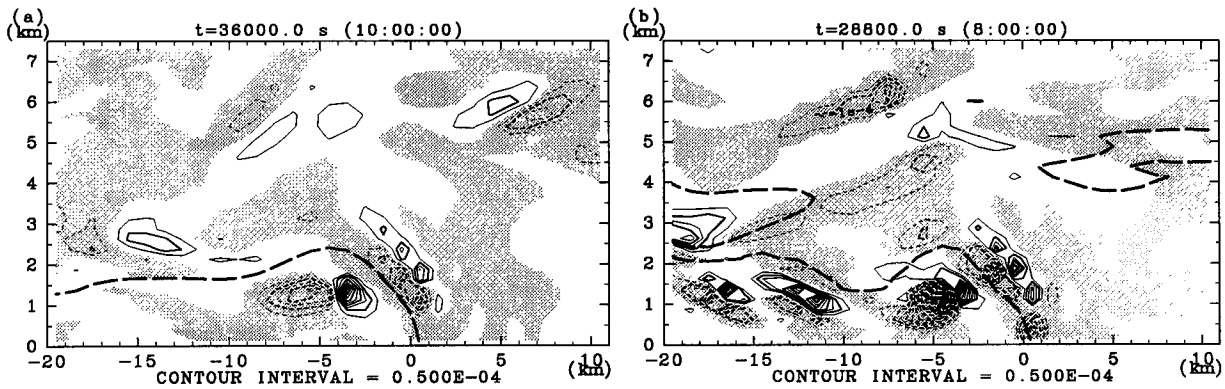

FIG. 4.17: The turbulent mixing term in the vertical momentum equation (a) at 10 h in CNTRL and (b) at 8h in DMLQV2. The contour interval is $5.0 \times 10^{-5}\,\mathrm{m^2\,s^{-1}}$ Negative values are shaded. $\theta' = -1\,\mathrm{K}$ is contoured by the dashed lines.

If the kinetic energy of a parcel is dissipated through this turbulent mixing, an additional energy is needed to lift the parcel to the LFC against the turbulent mixing. This energy required against the turbulent mixing probably works equivalently as CIN. The amount of this mixing can be dependent on

the length of the trajectory as well as the strength of the mixing. The large amount of the mixing is unfavorable for the initiation of convection. If the originating level within the ML is low (high), the parcel travels along a long (short) path near the cold pool's boundary before reaching the LFC, and thus experiences a large (small) amount of turbulent mixing.

The trajectories of parcels in the ML were affected by the cold pool depending on the source levels of the parcels. This is interpreted as the following two ways. First interpretation is connected with the low just above the cold pool. The relative location between the low and the parcel determines the magnitude of pressure gradient force, and thus controls the parcel trajectory. The parcels originating nearly the same levels as the peak of the low (eg., around $z = 2\,\mathrm{km}$ for CNTRL as shown in Fig. 4.4) are strongly affected by the pressure gradient force.

Second interpretation is obtained by considering horizontal vorticity component parallel to the squall line. Counterclockwise circulation is enhanced through baroclinic production of horizontal vorticity at the leading edge of the cold pool. The baroclinic generation $(-1/\rho^2\ \partial\rho/\partial x\ \partial p/\partial z)$ fields along with the system-relative flow vectors for CNTRL and DMLQV2 are shown in Fig. 4.18. A strong negative vorticity

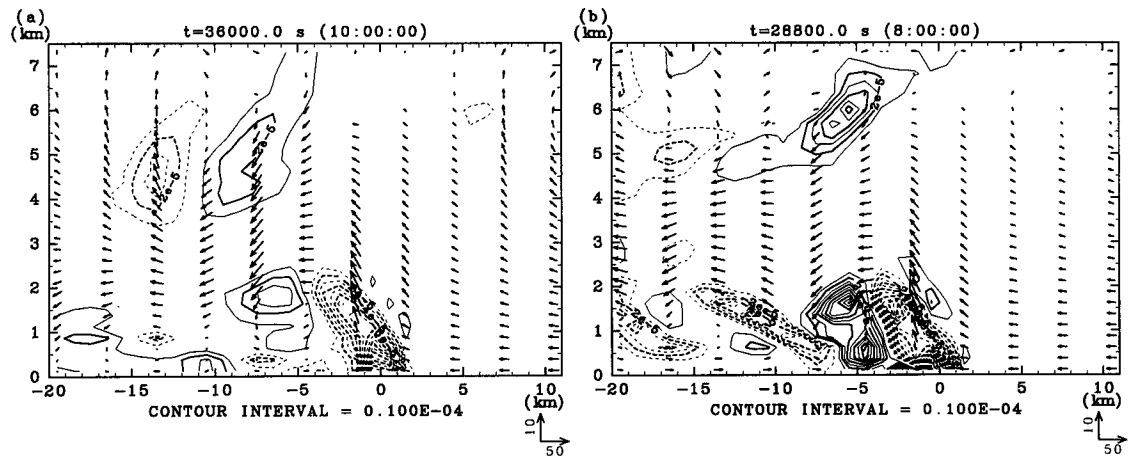

FIG. 4.18: Vertical cross sections of the system-relative flow vectors (the unit vector is indicated in the lower right corner) and baroclinic generation of horizontal vorticity (contoured every $1 \times 10^{-5}\,\mathrm{s}^{-2}$ with the zero contour omitted) for (a) CNTRL and (b) DMLQV2.

is forced at the leading edge of the cold pool for the both experiments. Because the magnitude of this negative vorticity is stronger than that inherent in the low-level shear, the paths of parcels originating in the lower part of the ML near the cold pool edge are strongly affected by the circulation induced by the cold pool. These parcels are hence tilted rearward (Rotunno et al. 1988). On the other hand, the parcels in the upper part of the ML will be less affected by the cold pool circulation (Fig. 4.18). Thus, these parcels can go upward if they have moderate CAPE values and little CIN.

Previous studies on the mechanism for the squall-line development and maintenance have emphasized

the relative importance between the horizontal vorticity generated by the cold pool and the horizontal vorticity inherent in the ambient low-level vertical shear (Thorpe et al. 1982; Rotunno et al. 1988; Weisman 1992). Rotunno et al. (1990) stressed that the balance between the vorticity inherent in the ambient shear and the vorticity generated by the cold pool is a necessary condition for sustaining strong, long-lived squall lines. However, in the present simulations the cold pool was very strong while the low-level shear was relatively weak: the optimum balance required to sustain the squall line (Rotunno et al. 1988) was not satisfied. Therefore, the physical process for releasing CAPE described here plays an important role in maintaining squall lines in dry conditions.

4.5 Comparison with the observation of the 5 May 1993 squall line

Table 4.2 summarizes the surface variables of the squall lines in the observation and the control experiment, both of which were in the mature stage. The comparison is restricted to the surface variables because of no available information on the detailed internal structure from the observation. In Table 4.2, the simulated results are significantly greater than the observations for the precipitation, the q_v increase, and the relative humidity of the cold pool, while the result is significantly smaller for the pressure rise. The greater values in the simulation are probably due to the two-dimensionality of the simulation. If an along-line variability is taken into account, mixing of squall line with ambient drier air in the along-line direction will be important. This mixing reduces the moisture content and relative humidity in the cold pool. Owing to this drier cold pool, the precipitation will be also reduced. The significant pressure rise in the observation possibly results from the tendency associated with the horizontally inhomogeneous state due to a synoptic cold front.

TABLE 4.2: Comparisons of surface variables between the observed squall line of 5 May 1993 and the simulated squall line in experiment CNTRL at $t = 10\,\mathrm{h}$.

	Max wind speed ($\mathrm{m\,s^{-1}}$)	Precipitation (mm)	θ decrease (K)	Pressure rise (Pa)	q_v increase ($\mathrm{g\,kg^{-1}}$)	Cold pool: Relative humidity (%)	Cold pool: Speed ($\mathrm{m\,s^{-1}}$)	Cold pool: Height (km)
Observation	21.8	< 0.1	16.9	760	1.9	34.8	~ 20	~ 2
CNTRL	26.3	0.8*	14.2	323	4.6	63.4	26.4*	1.51

* A value determined during 10-12h.

In spite of the quantitative discrepancies, the model well simulated in CNTRL the qualitative char-

acteristics associated with the passage of the gust front over the desert: very small rainfall; significant temperature drop; moistening; and fast movement of the cold pool. These similarities suggest that the maintenance mechanism of the 5 May 1993 squall line in China is inferred from the results of the present simulations.

4.6 Similarities with previous studies

As mentioned in section 4.2.2, the simulated squall line in CNTRL had an airflow similar to the up-down downdraft found over the High Plains by Knupp (1987). Knupp (1996) showed that a deep dry ABL, moderate wind shear, and a cold pool are required for the dominance of an up-down downdraft circulation. The present simulation satisfied these conditions: the present experiments seem to confirm Knupp's (1996) results. Furthermore, Knupp (1996) illustrated an airflow originating in the upper part of an ABL to become an updraft reaching upper levels. This airflow appears to be similar to trajectory B in Fig. 4.6a, and can be interpreted by the discussion presented in section 4.4 if we take into account the environmental conditions of the storm in Knupp's (1996) study. The airflow similar to trajectory A can be found in a High Plains squall line (Grady and Verlinde 1997).

The updrafts originating in the upper ML as well as the airflows similar to an up-down downdraft can be found in two-dimensional simulation of midlatitude squall lines investigated by Thorpe et al. (1982). They argued that the air nearest the surface ahead of a cold pool cannot easily be lifted to upper levels but enters the region of downdraft after lifted up by the cold-pool height, because the air has large horizontal momentum. This argument seems to be connected with our interpretation. It should be noted in the Thorpe et al. study that the origin of the inflow drawn into a descending region is limited to only near the surface, while the present experiments have shown that such inflow originates within the deeper layer in the lower ML.

Chapter 5

Synthesis and Conclusions

In the present study, the structure and evolution of the 5 May 1993 squall line over an arid region in China, and the mechanisms for development and maintenance of squall lines in dry environments have been investigated. The data acquired from routine observations and the HEIFE surface observations have been used to show the characteristics of the squall line that caused a severe dust storm. A simplified 1D model has been developed to investigate the evaporation of rain falling through a deep, dry ABL, and two-dimensional numerical experiments have been carried out by using a nonhydrostatic cloud model to investigate the dynamics of squall lines in dry conditions.

The observed squall line evolved in an extremely dry environment characterized by low surface q_v of less than $2.5\,\mathrm{g\,kg^{-1}}$ and a high LFC of about 5 km. The surface cold-air pool that emanated from the squall line propagated rapidly, producing strong convergence at its leading edge. In the pre-storm environment, a deep mixed layer developed, and its maximum depth was estimated as 4267 m.

The role played by a deep mixed layer in the squall-line evolution is proposed in the observational study. If the mixed layer is high, the difference between the height of the mixed-layer top and LFC is small. The energy required to lift the mixed-layer air above the LFC thus decreases. The cold surface outflow provides this lifting at its leading edge. Furthermore, the dry mixed layer is favorable for the evaporation of falling precipitation, thus enhancing the cold pool. In this way, the deep, dry mixed layer is a major cause to sustain deep convection at the leading edge of the cold pool.

One-dimensional modeling study of rain evaporation has shown that a significant amount of rain is depleted in a dry, deep mixed layer. If a constant amount of total rain is provided at the top of the model domain, the amount of evaporated rain increases with rain intensity. Thus, in severe convective clouds over arid regions, the rain falling bellow cloud bases is likely to evaporate completely in a subcloud layer.

The two-dimensional numerical experiments have focused on the sensitivity of the squall lines to low-level thermodynamic structure: the mixed-layer height and vertical profile of moisture within the mixed layer. The base states of the model have been characterized by low CAPE and high LFC. In the control experiment having the ML depth of 4375 m and ML moisture profile of nearly constant with height, a

persistent squall line is produced, in spite of the small amount of CAPE for the surface air parcel. The air parcels originating in the upper part of the mixed layer are raised to the upper troposphere during the mature stage of the squall line. On the other hand, air parcels originating in the lower part of the mixed layer are advected rearward, contributing to the intensification of the cold pool. In determining the parcel trajectories originating in the the mixed layer ahead of the cold pool, the low pressure just above the cold pool plays a significant role.

The sensitivity experiments in which the mixed-layer height and shape of the moisture profile within the mixed layer are varied illuminate the essential mechanisms for the development and maintenance of the simulated squall lines in dry environments. First, the presence of a deep mixed layer is indispensable for the squall-line development. Second, a moisture profile that is nearly constant with height is favorable for the long-lived squall lines, although the CAPE for the surface air parcel is not large (250 $J\,kg^{-1}$). In this moisture condition, air parcels in the upper part of the mixed layer have moderate CAPE (50-150 $J\,kg^{-1}$), and the differences between the source levels of these parcels and their LFC are very small. Thus, these parcels are easily lifted to their LFCs without experiencing substantial inhibition of convection, thus releasing their CAPE. On the other hand, the parcels in the lower mixed layer can not release their CAPE. The vertical distribution of CAPE in the mixed layer affects the dynamics of the squall line in dry environments. Squall lines can develop and persist if the mixed layer is sufficiently deep and if the moisture content within the mixed layer is well-mixed.

The long duration of the convective systems in the arid regions leads to long-lived severe storms. In China, there is a frequent cyclone formation in the northern arid region from April to May (Chen et al. 1991). Probably associated with these cyclones, dust storms are most frequent in this period (Parungo et al. 1994). Some of the dust storms are induced by a long-lived mesoscale convective system, similar to that described in chapter 2. Similarly, some duststorms in other arid regions are produced by convective systems. Severe dust storms have been reported also over the southwestern United States (Idso et al. 1972) and the Sudan (Lawson 1971; Morales 1981). If the environment satisfies the condition of a deep ML and well-mixed moisture profile, the storms can be long-lived owing to the persistent convective systems maintained by the mechanism described here. These environments are sometimes found in the arid region of China (Gamo 1996), the High Plains (Mahrt 1976; Wakimoto 1985), other arid regions (Gamo 1996), and also the Tibetan Plateau in summer (Yanai and Li 1994). Therefore, the mechanisms described in the present study can be applied to linearly-organized convective systems in these arid environments.

List of papers

本学位申請論文の基礎となった論文は以下の 4 篇である。

1. Structure and Evolution of a Severe Squall Line Over the Arid Region in Northwest China.

   Monthly Weather Review, in press, 1998

   Takemi, T.

2. 1993 年 5 月 5 日の中国北西部に発生したダストストームとその発生環境

   沙漠研究, **7**, 87-96, 1997

   竹見哲也

3. Evaporation of Rain Falling Bellow a Cloud Base Through a Deep Atmospheric Boundary Layer Over an Arid Region.

   Journal of the Meteorological Society of Japan, revised, 1998

   Takemi, T.

4. Numerical Experiments on the Mechanisms for the Development and Maintenance of Long-Lived Squall Lines in Dry Environments.

   Journal of the Atmospheric Sciences, submitted, 1998

   Takemi, T., and T. Satomura

Acknowledgment

I would like to thank Dr. Takehiko Satomura, my thesis advisor, for his valuable comments and constructive suggestions throughout the present work. His positive way of thinking always encourages me during my graduate research. I am very grateful to Dr. Hirohiko Ishikawa for his kind review of a manuscript (T98a) and continuous encouragement during my graduate course. I am also grateful to Professor Hiromasa Ueda for his interest in my research and his useful comments. I would like to thank Professors Hideji Kida and Tatsuya Iwashima for their comments at seminars. Thanks are due also to Dr. Taiichi Hayashi, Mr. Mitsuaki Horiguchi, and other colleagues at Disaster Prevention Research Institute, Kyoto University, including Dr. Ichiro Tamagawa (Nagoya University), Dr. Toru Nozawa (National Institute for Environmental Studies), and Dr. Toshihisa Itano (National Defense Academy), for their assistance on my graduate research.

I wish to give special thanks to Professors Emeritus Yoshi Sasaki of the University of Oklahoma and Yoshimitsu Ogura of the University of Illinois for their valuable comments and suggestions on the work described in chapter 2.

I am deeply grateful to Professor Emeritus Yasushi Mitsuta of Kyoto University for his valuable comments and continuous encouragement throughout my graduate research. I owe him a great deal for being what I am.

I acknowledge the support of a research fellowship for young scientists from the Japan Society for the Promotion of Science during my PhD course.

I am indebted to the participants of the HEIFE project for their efforts in observations, and to Lanzhou Institute of Plateau Atmospheric Physics and Gansu Provincial Meteorological Bureau for providing observational data and video records of the 5 May 1993 black storm. The HEIFE Program was sponsored jointly by Chinese Academy of Science, National Science Foundation of China, Gansu Province Government, and Ministry of Education, Science, Sports and Culture, Japan.

The numerical experiments presented in chapter 4 were made using the Advanced Regional Prediction System (ARPS) developed by the Center for Analysis and Prediction of Storms (CAPS), University of Oklahoma. CAPS is supported by the National Science Foundation and the Federal Aviation Administration through combined grant ATM92-20009. Dr. Alan Shapiro at CAPS is acknowledged to recommend to use the ARPS model.

The computation time was provided by the Supercomputing Laboratory, Institute for Chemical Research, Kyoto University, and the KDK system, Radio Atmospheric Science Center, Kyoto University.

Appendix A

The governing equations

In our two-dimensional numerical simulations, the model variables are written as follows:

$$u(x,z,t) = \overline{u}(z) + u'(x,z,t), \tag{A.1}$$

$$w(x,z,t) = w'(x,z,t), \tag{A.2}$$

$$\theta(x,z,t) = \overline{\theta}(z) + \theta'(x,z,t), \tag{A.3}$$

$$p(x,z,t) = \overline{p}(z) + p'(x,z,t), \tag{A.4}$$

$$\rho(x,z,t) = \overline{\rho}(z) + \rho'(x,z,t), \tag{A.5}$$

$$q_v(x,z,t) = \overline{q_v}(z) + {q_v}'(x,z,t), \tag{A.6}$$

$$q_{li}(x,z,t) = {q_{li}}'(x,z,t), \tag{A.7}$$

where u and w are the velocity components in the horizontal and vertical, respectively, θ the potential temperature, p the pressure, ρ the density, q_v the water vapor mixing ratio, and q_{li} one of the hydrometeor categories. The overbar denotes the base state variables and the prime the perturbation variables.

The base state atmosphere is assumed to satisfy the hydrostatic relation:

$$\frac{\partial \overline{p}}{\partial z} = -\overline{\rho} g. \tag{A.8}$$

The prognostic variables in the model are horizontal velocity u, vertical velocity w, potential temperature perturbation θ', pressure perturbation p', the six categories of water substance q_ψ (water vapor q_v, cloud water q_c, rainwater q_r, cloud ice q_i, snow q_s, and hail q_h).

The equation of state is given by

$$\rho = \frac{p}{R_d T}\left(1 - \frac{q_v}{\epsilon + q_v}\right)(1 + q_v + q_{li}) \tag{A.9}$$

where T is the air temperature, R_d the gas constant for dry air, and $\epsilon = R_d/R_v \approx 0.622$ is the ratio of the gas constant for dry air and water vapor.

The horizontal and vertical momentum equations are as follows:

$$\frac{\partial u}{\partial t} = -u\frac{\partial u}{\partial x} - w\frac{\partial u}{\partial z} - \frac{1}{\overline{\rho}}\frac{\partial p'}{\partial x} + D_u, \tag{A.10}$$

$$\frac{\partial w}{\partial t} = -u\frac{\partial w}{\partial x} - w\frac{\partial w}{\partial z} - \frac{1}{\overline{\rho}}\frac{\partial p'}{\partial z} + B + D_w, \tag{A.11}$$

where D_u and D_w represent the subgrid scale turbulent and computational mixing terms. B in the vertical momentum equation is the buoyancy term. The buoyancy B is given as follows:

$$B = -g\frac{\rho'}{\overline{\rho}} = g\left[\frac{\theta'}{\overline{\theta}} - \frac{p'}{\overline{\rho}c_s^2} + \frac{q_v'}{\epsilon + \overline{q_v}} - \frac{q_v' + q_{li}}{1 + \overline{q_v}}\right], \tag{A.12}$$

where $c_s \equiv \sqrt{\gamma R_d T}$ is the acoustic wave speed and $\gamma \equiv C_p/C_v$ is the ratio of the specific heat of air at constant pressure and volume.

The thermodynamic energy equation is

$$\frac{\partial \theta'}{\partial t} = -u\frac{\partial \theta'}{\partial x} - w\frac{\partial \theta'}{\partial z} - w\frac{\partial \overline{\theta}}{\partial z} + D_\theta + S_\theta, \tag{A.13}$$

where D_θ represents the subgrid scale turbulent mixing and S_θ the source/sink effects from microphysical processes.

The pressure perturbation is the prognostic variable in the continuity equation. This equation is given by

$$\frac{\partial p'}{\partial t} = -u\frac{\partial p'}{\partial x} - w\frac{\partial p'}{\partial z} + \overline{\rho}gw - \overline{\rho}{c_s}^2\left(\frac{\partial u}{\partial x} + \frac{\partial w}{\partial z}\right). \tag{A.14}$$

The conservation equations for the mixing ratio of water vapor, cloud water, rainwater, cloud ice, snow, and hail are given in a general form for a variable q_ψ as

$$\frac{\partial q_\psi}{\partial t} = -u\frac{\partial q_\psi}{\partial x} - w\frac{\partial q_\psi}{\partial z} - \frac{1}{\overline{\rho}}\frac{\partial}{\partial z}(\overline{\rho}V_{q_\psi}q_\psi) + D_{q_\psi} + S_{q_\psi}, \tag{A.15}$$

where D_{q_ψ} and S_{q_ψ} represent the subgrid scale turbulent mixing term and the source/sink terms, and V_{q_ψ} is the terminal fall velocities for rain, snow and hail.

References

Bluestein, H. B. and M. H. Jain, 1985: Formation of mesoscale lines of precipitation: severe squall lines in Oklahoma during the spring. *J. Atmos. Sci.*, **42**, 1711-1732.

Bluestein, H. B., G. T. Marx, and M. H. Jain, 1987: Formation of mesoscale lines of precipitation: Nonsevere squall lines in Oklahoma during the spring. *Mon. Wea. Rev.*, **115**, 2719-2727.

Braham, Jr, R. R., 1952: The water and energy budgets of the thunderstorm and their relation to thunderstorm development. *J. Meteor.*, **9**, 227-242.

Broccoli, A. J., S. Manabe, 1992: The effects of orography on midlatitude Northern Hemisphere dry climates. *J. Climate*, **5**, 1181-1201.

Chen, S. -J., Y. -H. Kuo, P. -Z. Zhang, and Q. -F. Bai, 1991: Synoptic climatology of cyclogenesis over east Asia, 1958-1987. *Mon. Wea. Rev.*, **119**, 1407-1418.

Colby, F. P., Jr., 1984: Convective inhibition as a predictor of convection during AVE-SESAME II. *Mon. Wea. Rev.*, **112**, 2239-2252.

Crook, N. A., 1996: Sensitivity of moist convection forced by boundary layer processes to low-level thermodynamic fields. *Mon. Wea. Rev.*, **124**, 1767-1785.

Doty, K. G., and D. J. Perkey, 1993: Sensitivity of trajectory calculations to the temporal frequency of wind data. *Mon. Wea. Rev.*, **121**, 387-401.

Droegemeier, K. K., and R. B. Wilhelmson, 1985: Three-dimensional numerical modeling of convection produced by interacting thunderstorm outflows. Part I: Control simulation and low-level moisture variations. *J. Atmos. Sci.*, **42**, 2381-2403.

Dudhia, J., M. W. Moncrieff, and D. W. K. So, 1987: The two-dimensional dynamics of west African squall lines. *Quart. J. Roy. Meteor. Soc.*, **113**, 121-146.

Emanuel, K. A., 1994: *Atmospheric Convection.* Oxford University Press, 580 pp.

Fankhauser, J. C., G. M. Barnes, and M. A. LeMone, 1992: Structure of a midlatitude squall line formed in strong unidirectional shear. *Mon. Wea. Rev.*, **120**, 237-260.

Farquharson, J. S., 1937: Haboobs and instability in the Sudan. *Quart. J. Roy. Meteor. Soc.*, **63**, 393-414.

Fovell, R. G., and Y. Ogura, 1988: Numerical simulation of a midlatitude squall line in two dimensions. *J. Atmos. Sci.*, **45**, 3846-3879.

Fovell, R. G., and Y. Ogura, 1989: Effects of vertical wind shear on numerically simulated multicell storm structure. *J. Atmos. Sci.*, **46**, 3144-3176.

Fovell, R. G., and P. -H. Tan, 1998: The temporal behavior of numerically simulated multicell-type storms. Part II: The convective cell life cycle and cell regeneration. *Mon. Wea. Rev.*, **126**, 551-577.

Fujita, T. T., and R. M. Wakimoto, 1981: Five scales of airflow associated with a series of downbursts on 16 July 1980. *Mon. Wea. Rev.*, **109**, 1438-1456.

Gamo, M., 1996: Thickness of the dry convection and large-scale subsidence above deserts. *Bound.*

-Layer Meteor., **79**, 265-278.

Garratt, J. R., 1992: *The Atmospheric Boundary Layer*, Cambridge University Press, 316 pp.

Garner, S. T., and A. J. Thorpe, 1992: The development of organized convection in a simplified squall-line model. *Quart. J. Roy. Meteor. Soc.*, **118**, 101-124.

Grady, R. L., and J. Verlinde, 1997: Triple-doppler analysis of a discretely propagating, long-lived High Plains squall line. *J. Atmos. Sci*, **54**, 2729-2748.

Hartmann, D. L., 1994: *Global Physical Climatology*, Academic Press, 411 pp.

Holzworth, G. C., 1964: Estimates of mean maximum mixing depths in the contiguous United States. *Mon. Wea. Rev.*, **92**, 235-242.

Houze, R. A., S. A. Rutledge, M. I. Biggerstaff, and B. F. Smull, 1989: Interpretation of doppler weather radar displays of midlatitude mesoscale convective system. *Bull. Amer. Meteor. Soc.*, **70**, 608-619.

Houze, R. A., Jr., B. F. Smull, and P. Dodge, 1990: Mesoscale organization of springtime rainstorms in Oklahoma. *Mon. Wea. Rev.*, **118**, 613-654.

Huschke, R. E., Ed., 1959: *Glossary of Meteorology*, Amer. Meteor. Soc., 638 pp.

Idso, S. B., R. S. Ingram, and J. M. Pritchard, 1972: An American haboob. *Bull. Amer. Meteor. Soc.*, **53**, 930-935.

Itano, T., 1997: Rainfall over the arid area in the northwestern China. -An analysis during HEIFE-, *J. Meteor. Soc. Japan*, **75**, 851-865.

Itano, T., 1998: Synoptic disturbance and rainfall over the arid area in the northwestern China. *J. Meteor. Soc. Japan*, **76**, 325-333.

Johns, R. H., and W. D. Hirt, 1987: Derechos: widespread convectively induced windstorms. *Wea. Forecasting*, **2**, 32-49.

Kamburova, P. L., and F. H. Ludlam, 1966: Rainfall evaporation in thunderstorm downdraughts. *Quart. J. Roy. Meteor. Soc.*, **92**, 510-518.

Kato, K., H. Iwasaki, J. Matsumoto, 1992: A preliminary report on the water cycle around the arid and semiarid area in East Asia. *Tenki*, **39**, 408-413. (in Japanese)

Kessler, E., 1969: On the distribution and continuity of water substance in atmospheric circulations., *Meteor. Monogr.*, **10**

Klemp, J. B., and R. B. Wilhelmson, 1978: The simulation of three-dimensional convective storm dynamics. *J. Atmos. Sci.*, **35**, 1070-1096.

Knupp, K. R., 1987: Downdrafts within High Plains cumulonimbi. Part I: General kinematic structure. *J. Atmos. Sci.*, **44**, 987-1008.

Knupp, K. R., 1996: Structure and evolution of a long-lived, microburst-producing storm. *Mon. Wea. Rev.*, **124**, 2785-2806.

Krumm, W. R., 1954: On the cause of downdrafts from dry thunderstorm over the plateau area of the United States. *Bull. Amer. Meteor. Soc.*, **35**, 122-125.

Lafore, J. P.,and M. W. Moncrieff,1989: A numerical investigation of the organization and interaction of the convective and stratiform regions of tropical squall lines. *J. Atmos. Sci.*, **46**, 521-544.

Lawson, T. J., 1971: Haboob structure at Khartoum. *Weather*, **26**, 105-112.

Leary, C. A., 1980: Temperature and humidity profiles in mesoscale unsaturated downdrafts. *J. Atmos. Sci.*, **37**, 1005-1012.

Lin, Y. -L., R. D. Farley, and H. D. Orville, 1983: Bulk parameterization of the snow field in a cloud model. *J. Climate Appl. Meteor.*, **22**, 1065-1092.

Mahrt, L., 1976: Mixed layer moisture structure. *Mon. Wea. Rev.*, **104**, 1403-1407.

Marshall, J. S., and W. M. Palmer, 1948: The distribution of raindrops with size. *J. Meteor.*, **5**, 165-166.

Mattice, W. A., 1935: Dust storms, November 1933 to May 1934. *Mon. Wea. Rev.*, **63**, 53-55.

Mitsuta, Y, 1988: Sino-Japanese cooperational program on the atmosphere-land surface processes. *Tenki*, **35**, 501-505. (in Japanese)

Mitsuta, Y., I. Tamagawa, K. Sahashi, and J. Wang, 1995a: Estimation of annual evaporation from the Linze Desert during HEIFE. *J. Meteor. Soc. Japan*, **73**, 967-974.

Mitsuta, Y., T. Hayashi, T. Takemi, Y. Hu, J. Wang, and M. Chen, 1995b: Two severe local storms as observed in the arid area of northwest China. *J. Meteor. Soc. Japan*, **73**, 1269-1284.

Morales, H. C., 1981: A case study of a dust storm weather situation in the Sudan in April 1973. *PAGEOPH*, **119**, 658-676.

Nalivkin, D. V., 1983: *Hurricanes, Storms and Tornadoes.* A. A. Balkema., Rotterdam.

Newton, C. W., 1950: Structure and mechanism of the prefrontal squall line., *J. Meteor.*, **7**, 210-222.

Newton, C. W., and H. R. Newton, 1959: Dynamic interactions between large convective clouds and environment with vertical shear. *J. Meteor.*, **16**, 483-496.

Nicholls, M. E., R. H. Johnson, and W. R. Cotton, 1988: The sensitivity of two-dimensional simulations of tropical squall lines to environmental profiles. *J. Atmos. Sci.*, **45**, 3625-3649.

Ogura, Y. and T. Takahashi, 1971: Numerical simulation of the life cycle of a thunderstorm cell. *Mon. Wea. Rev.*, **99**, 895-911.

Ogura, Y., and Y. -L. Chen, 1977: A life history of an intense mesoscale convective storm in Oklahoma. *J. Atmos. Sci.*, **34**, 1458-1476.

Ogura, Y., and M. -T. Liou, 1980: The structure of a midlatitude squall line: a case study. *J. Atmos. Sci.*, **37**, 553-567.

Ohno, H., 1994: Gust fronts in Niger., *Tenki*, **41** (in Japanese)

Orlanski, I., 1976: A simple boundary condition for unbounded hyperbolic flows. *J. Comput. Phys.*, **21**, 251-269.

Parungo, F., Z. Li, X. Li, D. Yang, and J. Harris, 1994: Gobi dust storms and the Great Green Wall. *Geophys. Res. Lett.*, **21**, 999-1002.

Rosenfeld, D., and Y. Mintz, 1988: Evaporation of rain falling from convective clouds as derived from

radar measurements. *J. Appl. Meteor.*, **27**, 209-215.

Rotunno, R., J. B. Klemp, and M. L. Weisman, 1988: A theory for strong, long-lived squall lines. *J. Atmos. Sci.*, **45**, 463-485.

Rotunno, R., J. B. Klemp, and M. L. Weisman, 1990: Comments on "A numerical investigation of the organization and interaction of the convective and stratiform regions of tropical squall lines" *J. Atmos. Sci.*, **47**, 1031-1033.

Ryan, B. F. and J. C. Carstens, 1978: A comparison between a steady-state downdraft model and observations behind squall lines. *J. Appl. Meteor.*, **17**, 395-400.

Sahashi, K., 1995: A wet period in the Desert Station in HEIFE. *J. Meteor. Soc. Japan*, **73**, 1213-1217.

Sawyer, J. S., 1946: Cooling by rain as a cause of the pressure rise in convectional squalls. *Quart. J. Roy. Meteor. Soc.*, **72**, 168.

Schmidt, J. M., and W. R. Cotton, 1989: A high plains squall line associated with severe surface winds. *J. Atmos. Sci.*, **46**, 281-302.

Simpson, J. E., 1969: A comparison between laboratory and atmospheric density currents. *Quart. J. Roy. Meteor. Soc.*, **95**, 758-765.

Skamarock, W. C., M. L. Weisman, and J. B. Klemp, 1994: Three-dimensional evolution of simulated long-lived squall lines. *J. Atoms. Sci.*, **51**, 2563-2584.

Smull, B. F., and R. A. Houze, Jr., 1987: Rear inflow in squall lines with trailing stratiform precipitation. *Mon. Wea. Rev.*, **115**, 2869-2889.

Soong, S. -T., and Y. Ogura, 1973: A comparison between axisymmetric and slab-symmetric cumulus cloud models. *J. Atmos. Sci.*, **30**, 879-893.

Srivastava, R. C., 1985: A simple model of evaporatively driven downdraft: Application to microburst downdraft. *J. Atmos. Sci.*, **42**, 1004-1023.

Sutton, L. J., 1925: Haboobs. *Quart. J. Roy. Meteor. Soc.*, **51**, 25-30.

Syono, S., and T. Takeda, 1962: On the evaporation of raindrops in a sub-cloud layer. *J. Meteor. Soc. Japan*, **40**, 245-265.

Takemi, T., 1997: The 5 May 1993 Dust Storm over the Northwestern China and the Environmental Condition of Its Development. *J. Arid Land Studies*, **7**, 87-96. (in Japanese)

Takemi, T., 1998a: Structure and evolution of a severe squall line over the arid region in northwest China. *Mon. Wea. Rev.*, in press.

Takemi, T., 1998b: Evaporatively depleted rain falling bellow a cloud base through the deep, dry atmospheric boundary layer over an arid region. *J. Meteor. Soc. Japan*, revised.

Takemi, T., and T. Satomura, 1998: Numerical experiments on the Mechanisms for the development and maintenance of long-lived squall lines in dry environments. *J. Atmos. Sci.*, submitted.

Thorpe, A. J., M. J. Miller, and M. W. Moncrieff, 1982: Two-dimensional convection in non-constant shear: a model of mid-latitude squall lines. *Quart. J. Roy. Meteor. Soc.*, **108**, 739-762.

Wakimoto, R. M., 1985: Forecasting dry microburst activity over the High Plains. *Mon. Wea. Rev.*, **113**, 1131-1143.

Weisman, M. L., 1992: The role of convectively generated rear-inflow jets in the evolution of long-lived mesoconvective systems. *J. Atmos. Sci.*, **49**, 1826-1847.

Weisman, M. L., J. B. Klemp, and R. Rotunno, 1988: Structure and evolution of numerically simulated squall lines. *J. Atmos. Sci.*, **45**, 1990-2013.

Williams, E., and N. Renno, 1993: An analysis of the conditional instability of the tropical atmosphere. *Mon. Wea. Rev.*, **121**, 21-36.

Xue, M., K. K. Droegemeier, V. Wong, A. Shapiro, K. Brewster, 1995: ARPS Version 4.0 User's Guide, CAPS, University of Oklahoma, 380 pp. [Available from CAPS, University of Oklahoma, Norman OK 73019, USA].

Yanai, M., and C. Li, 1994: Mechanism of heating and the boundary layer over the Tibetan Plateau. *Mon. Wea. Rev.*, **122**, 305-323.

Yatagai, A., and T. Yasunari, 1995: Interannual variations of summer precipitation in the arid/semi-arid regions in China and Mongolia: Their regionality and relation to the Asian summer monsoon. *J. Meteor. Soc. Japan*, **73**, 909-923.

Zipser, E. J., 1977: Mesoscale and convective-scale downdrafts as distinct components of squall-line structure. *Mon. Wea. Rev.*, **105**, 1568-1589.